CHARACTERIZATION OF DAMAGE DUE TO STRESS CORROSION CRACKING IN CARBON STEEL USING NONLINEAR SURFACE ACOUSTIC WAVES

A Thesis
Presented to
The Academic Faculty

by

Daniel T. Zeitvogel

In Partial Fulfillment
of the Requirements for the Degree
Master of Science in
Engineering Science and Mechanics

School of Civil and Environmental Engineering
Georgia Institute of Technology
December 2012

CHARACTERIZATION OF DAMAGE DUE TO STRESS CORROSION CRACKING IN CARBON STEEL USING NONLINEAR SURFACE ACOUSTIC WAVES

Approved by:

Professor Laurence J. Jacobs, Advisor
School of Civil and Environmental Engineering
Georgia Institute of Technology

Dr. Jin-Yeon Kim
School of Civil and Environmental Engineering
Georgia Institute of Technology

Dr. Jianmin Qu
Department of Civil and Environmental Engineering
Northwestern University

Date Approved: August 23 2012

ACKNOWLEDGEMENTS

First of all, I want to thank my advisor Prof. Laurence J. Jacobs, for the support and motivation he gave me throughout my stay in Atlanta. Apart from making it possible to come to Georgia Tech to write this thesis, he also gave me the opportunity to present the results of this thesis at the QNDE 2012 in Denver. Furthermore, I want to thank Dr. Jin-Yeon Kim for the practical and intellectual help he gave me, without which I would never have managed to finish my thesis. I also want to thank Dr. Jianmin Qu from Northwestern University for reviewing my thesis and serving as a committee member.

Moreover, I want to thank Prof. Preet M. Singh and Dr. Jamshad Mahmood, for giving me valuable insights in the field of material science and for letting me use and assisting me in the use of their equipment.

I also want to thank Dr. Peter Cawley and Joseph Corcoran from Imperial College for conducting complimentary measurements.

This study program was made possible by a long standing cooperation between Prof. Laurence J. Jacobs and the Institute of Applied and Experimental Mechanics at the University of Stuttgart. I want to thank particularly Prof. Lothar Gaul and Dr. Jan Herrmann for organizing this exchange program.

Further thanks go to my fellow students in the lab, who made this year interesting, informative, and entertaining and were very helpful in writing this thesis: Katie Matlack, Johann Groß, Christian Swacek, Chi-Luen Huang, and Rachel Devine. Last but not least, I want to thank my friends in Germany who stayed in touch with me. Special thanks go to my family, who gave me a lot of motivation and supported me during the whole stay.

TABLE OF CONTENTS

LIST OF TABLES

LIST OF FIGURES

LIST OF SYMBOLS

Symbol	Description
A, B	amplitudes
A_1	amplitude of the fundamental frequency
A_2	amplitude of the second harmonic
c	wave speed
C_{ijkl}	fourth order stiffness tensor
c_L, c_T, c_R	longitudinal, transverse and Rayleigh wave speed
C	constant
$\mathbf{d}$	direction of particle motion
E	Young's modulus
E_{ij}	Lagrangian strain tensor
f	frequency
f_i	body forces
F_{ij}	deformation gradient tensor
i	imaginary unit
k	wavenumber
n_j	normal vector
$\mathbf{p}$	unit vector in direction of propagation
p_{dmg}	damage parameter
P_{ij}	Piola-Kirchhoff stress tensor
S	surface
t_i	traction
u_i	displacement
V	volume
W	strain energy

Symbol	Description
x	propagation distance
$\mathbf{x}$	position vector
X_j	Lagrangian coordinate
z	constant
β	nonlinearity parameter
δ_{ij}	Kronecker delta
ϵ_{ij}	strain tensor
Θ	angle of incident / reflected wave
λ	wavelength
λ, μ	Lamé constants
ν	Poisson's ratio
ρ	density
σ_{ij}	stress tensor
σ_{yield}	yield strength
σ_{ult}	ultimate tensile strength
φ, θ	displacement potentials
ω	angular frequency
∇	Nabla operator

SUMMARY

Cold rolled carbon steel 1018C is widely used in pressurized fuel pipelines. For those structures, stress corrosion cracking (SCC) can pose a significant problem because cracks initiate late in the lifetime and often unexpectedly, but grow fast once they get started. To ensure a safe operation, it is crucial that any damage can be detected before the structural stability is reduced by large cracks. In the early stages of SCC, microstructural changes occur which increase the acoustic nonlinearity of the material. Therefore, an initially monochromatic Rayleigh wave is distorted and measurable higher harmonics are generated. Different levels of stress corrosion cracking is induced in five specimens. For each specimen, nonlinear ultrasonic measurements are performed before and after inducing the damage. For the measurements, oil coupled wedge transducers are used to generate and detect tone burst Rayleigh wave signals. The amplitudes of the received fundamental and second harmonic waves are measured at varying propagation distances to obtain a measure for the acoustic nonlinearity of the material. The results show a damage-dependent increase in nonlinearity for early stages of damage, indicating the suitability for this nonlinear ultrasonic method to detect stress corrosion cracking before structural failure.

CHAPTER I

INTRODUCTION

1.1 Motivation and Objectives

Cold finished carbon steels like 1018C are widely used for buried pipelines for gasoline transport. The surrounding soil presents a mildly corrosive environment which under normal circumstances poses only small risk for the pipelines. However, due to tensile stresses which result from a combination of residual stress from welded joints and pressure inside the pipe, stress corrosion cracking can occur [14]. Stress corrosion cracking poses great risk to those structures because it often occurs unexpectedly. First of all, it can occur to materials and in environments that seem innocuous at first glance [18]. Furthermore, the cracks initiate rather late in the lifetime of a structure, but grow very fast once initiated. Therefore, it is desirable to detect the beginning of stress corrosion damage as soon as possible, preferably before macrocracks form. While macrocracks can be detected by linear ultrasonic measurements and eddy currents [5], those detection methods are less suitable for the detection of microcracks and microstructural changes. Nonlinear ultrasonic methods, however, are capable of detecting microstructural changes as dislocations and other changes in the material condition distort ultrasonic waves and generate higher harmonic waves. Different kinds of ultrasonic waves can be used for this kind of measurement. As stress corrosion cracking generally starts at the surface, it is advantageous to use Rayleigh surface waves, which travel farther than bulk waves and their energy is concentrated near the free surface of the material.

The objective of this research is to develop a method to detect stress corrosion cracking in 1018C steel based on nonlinear ultrasonic measurements with varying propagation

distances. This method is then used to characterize the nonlinear behavior of 1018C steel with regard to the amount of stress corrosion damage.

1.2 Previous Work

Linear ultrasonic measurements have long been used to detect material defects like cavities or large cracks. Evaluation methods for linear ultrasonic measurements include time of flight, attenuation, reflection, and mode conversion measurements. While these methods are reliable for damage types that are large enough to cause measurable changes in the ultrasonic wave, they are less suitable to detect changes in the microstructure of the material. In the past several years, a number of analytical and experimental research was done in the field of nonlinear ultrasonics, as this technique makes it possible to detect changes in the microstructure. Cantrell [2] showed analytically that microstructural changes in face-centered-cubic metals create a change in the nonlinearity parameter. Numerous experimental approaches using longitudinal nonlinear ultrasonic waves have been used to detect material damage, particularly fatigue damage. This was done by Nagy [15], who measured fatigue damage in various materials, including aluminum, titanium, and plastics, and Cantrell [3], who measured fatigue damage in aluminum. Other kinds of damage can also be detected using longitudinal nonlinear ultrasonic waves, as shown by Valluri [24], who detected creep damage in copper. Nonlinear guided waves offer a wide spectrum of applications: Pruell [19] used nonlinear Lamb waves as to detect fatigue damage in aluminum. As mentioned earlier, Rayleigh surface waves have many advantages when the damage is concentrated near the surface. They have been used by Herrmann [8] to detect fatigue damage in a nickel-based superalloy and by Walker [27] to detect fatigue damage in A36 steel. Nonlinear Rayleigh surface waves have also been used by Liu [13] to measure residual stress in shot-peened aluminum plates. Matlack [14] used nonlinear Rayleigh surface waves to measure damage due to stress corrosion

cracking in carbon steel. This is used as a basis for the research done in this thesis.

1.3 Structure of the Thesis

In Chapter 2, the theory of wave propagation and wave phenomena are discussed, with special regards to nonlinear wave propagation and Rayleigh surface waves. The mechanisms of stress corrosion cracking are presented in Chapter 3. This chapter also outlines the methods used to induce damage in the specimens and the optical microscopic examination of the damaged specimens. In Chapter 4, the properties of the specimens are presented. Then, an overview of the procedure of ultrasonic measurements is given, before the results of preliminary tests of the material properties are presented. The results of the nonlinear ultrasonic measurements are discussed in Chapter 5. First, the results of the tests are presented separately for each specimen, then the obtained results are compared. Finally, in Chapter 6, a conclusion is drawn.

CHAPTER II

WAVE PROPAGATION IN SOLIDS

In this chapter, wave propagation in elastic solids will be discussed. After deriving the equations of motion, the concepts of linear wave propagation phenomena will be discussed.

2.1 Equation of Motion

As explained in [1], a good point to start is the balance of linear momentum

$$\int_S t_i \mathrm{d}S + \int_V \rho f_i \mathrm{d}V = \int_V \rho \ddot{u}_i \mathrm{d}V \tag{2.1}$$

where S and V are the surface and volume, respectively, of a closed region of a body which is exposed to a surface traction t_i and a body force f_i. By substituting the Cauchy stress formula

$$t_i = \sigma_{ki} n_k \tag{2.2}$$

into (2.1) and making use of Gauss' theorem to transform the surface integral into a volume integral, we obtain

$$\int (\sigma_{ij,j} + \rho f_i - \rho \dot{v}_i) \mathrm{d}V = 0. \tag{2.3}$$

Because V can be arbitrary, we get Cauchy's first law of motion for a continuus integrand

$$\sigma_{ij,i} + \rho f_i = \rho \ddot{u}_i. \tag{2.4}$$

However, it is sometimes desirable to use an equation of motion which is independent of stress and only depends on material constants and displacement. Assuming a homogenous, isotropic, linearly elastic solid, strain and stress can be related by Hooke's

law

$$\sigma_{ij} = \lambda \epsilon_{kk} \delta_{ij} + 2\mu \epsilon_{ij} \tag{2.5}$$

with Lamé's elastic constants λ and μ, which can be obtained from the material properties Young's modulus E and Poisson's ratio ν by

$$\lambda = \frac{E\nu}{(1+\nu)(1-2\nu)} \tag{2.6}$$

$$\mu = \frac{E}{2(1+\nu)}. \tag{2.7}$$

Furthermore, strain is defined by

$$\epsilon_{ij} = \frac{1}{2}(u_{i,j} + u_{j,i}). \tag{2.8}$$

Substituting (2.5) and (2.8) into (2.4) to eliminate the stress and neglecting body forces, we obtain Navier's equation of motion

$$(\lambda + \mu) u_{j,ji} + \mu u_{i,ji} = \rho \ddot{u}_i \tag{2.9}$$

which can also be written in vector representation

$$\mu \nabla^2 \mathbf{u} + (\lambda + \mu) \nabla \nabla \cdot \mathbf{u} = \rho \ddot{\mathbf{u}}. \tag{2.10}$$

In a three-dimensional environment, this represents a set of three coupled partial differential equations. For multi-dimensional wave propagation, we can introduce a scalar potential φ and a vector potential ψ, so that

$$\mathbf{u} = \nabla \varphi + \nabla \times \psi. \tag{2.11}$$

In order to be able to uniquely obtain the three components of $\mathbf{u}$ from the four components of φ and ψ, the additional condition

$$\nabla \cdot \psi = 0 \tag{2.12}$$

has to be fulfilled. Substituting (2.11) and (2.12) in (2.10) eventually leads us to

$$(\lambda + 2\mu) \nabla^2 \varphi = \rho \ddot{\varphi} \tag{2.13}$$

and

$$\mu \nabla \psi = \rho \ddot{\psi}, \tag{2.14}$$

which are uncoupled equations in terms of φ and ψ. Introducing the longitudinal wave speed c_L and the transverse wave speed c_T yields the uncoupled wave equations

$$\nabla^2 \varphi = \frac{1}{c_L^2} \ddot{\varphi} \tag{2.15}$$

and

$$\nabla^2 \psi = \frac{1}{c_T^2} \ddot{\psi} \tag{2.16}$$

which represent longitudinal waves and vertically and horizontally polarized shear waves.

2.2 Linear Wave Propagation

2.2.1 Plane Waves

In this section, we will assume plane waves, i.e., waves which have constant values of properties such as displacement $\mathbf{u}$, strain ϵ, and stress σ on each plane perpendicular to the unit propagation vector $\mathbf{p}$. With the unit particle motion vector $\mathbf{d}$, such a wave can be described by

$$\mathbf{u} = f(\mathbf{x} \cdot \mathbf{p} - ct)\mathbf{d}, \tag{2.17}$$

where c can be either the longitudinal wave speed c_L or the transverse wave speed c_T. By substituting (2.17) into eq. (2.10), we get

$$(\mu - \rho c^2)\mathbf{d} + (\lambda + \mu)(\mathbf{p} \cdot \mathbf{d})\mathbf{p} = 0. \tag{2.18}$$

Seeing that $\mathbf{p}$ and $\mathbf{d}$ are two unit vectors, there are only two cases for which this equation can be satisfied:

1. $\mathbf{d} = \pm\mathbf{p}$, so $\mathbf{p} \cdot \mathbf{d} = 1$. This means that the wave propagates in the same direction as the particle movement, which is known as a longitudinal wave (P-wave). In

this case, (2.18) can be solved for the longitudinal wave speed

$$c = c_L = \sqrt{\frac{\lambda + 2\mu}{\rho}}. \tag{2.19}$$

2. $\mathbf{p} \cdot \mathbf{d} = 0$. This means that the wave propagates exactly orthogonal to the particle movement, which is known as a shear wave. Assuming that the wave propagates in a two-dimensional plane (usually the x_1x_2-plane), a vertically polarized shear wave (SV-wave) has particle motion in the x_1x_2-plane, whereas a horizontally polarized shear wave has particle motion only in the x_3-direction. For a shear wave, (2.18) can be solved for the transverse wave speed

$$c = c_T = \sqrt{\frac{\mu}{\rho}}. \tag{2.20}$$

Comparing (2.19) and (**??**, it becomes obvious that $c_L > c_T$ is always true, which means that in a given material, the longitudinal wave always propagates faster than the shear wave.

In many cases, it is useful to consider waves with a time harmonic behavior. Such a wave with the amplitude A, which can be real-valued or complex, but not depending on neither x nor t, can be represented by

$$\mathbf{u}^{(n)} = A_n \mathbf{d}^{(n)} \exp\left[\mathrm{i}k_n \left(x_1 p_1^{(n)} + x_2 p_2^{(n)} - c_n t\right)\right]. \tag{2.21}$$

n represents the wave type (i.e., longitudinal or shear wave) with the corresponding wave properties propagation velocity c_n and wave number $k_n = \frac{\omega}{c_n}$, where $\omega = \frac{2\pi}{T}$ is the circular frequency. $\mathbf{d}^{(n)}$ is the unit vector of the wave's particle motion.

2.2.2 Wave Reflection at a Stress Free Boundary

The above considerations were made in assumption of an infinite medium. In reality, however, waves are likely to encounter boundaries. In the general case of a boundary between two media, reflection as well as transmission occur. At a free boundary, which is a boundary between a medium and vacuum (or, idealized, air), there is

no transmission, but only reflection, so all energy stays in the medium. The stress-free boundary conditions for a wave propagating in the x_1x_2-plane, with a boundary orthogonal to the x_2-axis, are $\sigma_{22} = 0$ and $\sigma_{12} = 0$. One distinctive feature of reflection at a boundary is the so-called mode conversion, which means that for an incident P-wave or SV-wave, there will generally be both a reflected P-wave as well as an SV-wave as shown in Figure 2.1. For an incident SH-wave, however, only an SH-wave will be reflected.

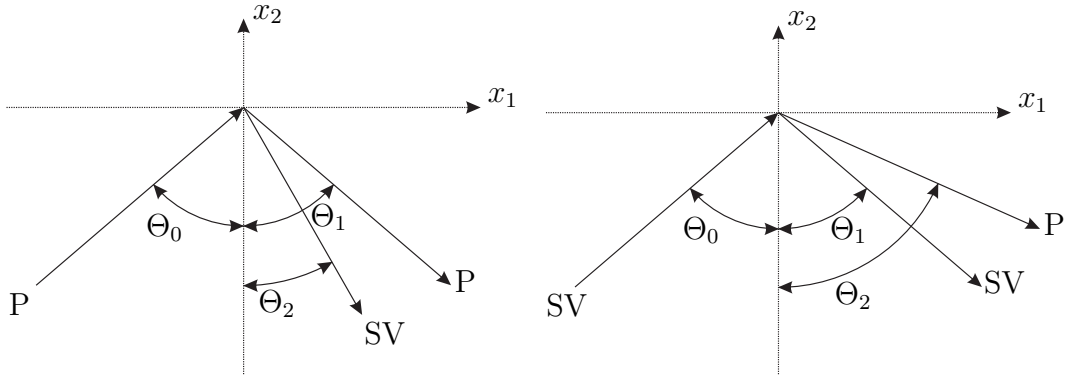

Figure 2.1: Reflection of P-wave and SV-wave

Assuming a constant linear frequency for incident and reflected waves, we can use (2.21) to obtain a relationship between the angle of the incident wave, θ_0, and the angles of the reflected waves, θ_1 and θ_2 as shown in Table 2.1.

Table 2.1: Relationships between the angles of incident and reflected waves

Incident θ_0	Reflected P θ_1	Reflected SV θ_2
P	$\theta_1 = \theta_0$	$\sin\theta_2 = (c_T/c_L)\sin\theta_0$
SV	$\sin\theta_1 = (c_L/c_S)\sin\theta_0$	$\theta_2 = \theta_0$

The angles of the incident and reflected waves, θ_0, θ_1, and θ_2 have to satisfy Snell's law,

$$k_0 \sin\theta_0 = k_1 \sin\theta_1 = k_2 \sin\theta_2 \tag{2.22}$$

in order to obtain non-trivial amplitudes A_n. There are two cases for which no mode conversion occurs:

- $\theta_0 = 0$, i.e. the incident wave is orthogonal to the boundary. In this case, the wave will be reflected as itself.

- $\theta_0 > \theta_{critical}$ for an incident P-wave, where $\theta_{critical} = \arcsin \frac{c_T}{c_L}$ is the shear wave critical angle. In this case, only an SV-wave is reflected, while the P-wave portion of the reflection generates a Rayleigh surface wave. This type of surface wave will be used in this research.

2.3 Rayleigh Surface Waves

2.3.1 Properties of Rayleigh Waves

Rayleigh waves are surface waves, which means they travel along the free surface of an elastic half-space with the amplitude decaying exponentially with depth. The mathematical description is derived in detail by Viktorov [25] and Achenbach [1]. Applications of Rayleigh waves in ultrasonic nondestructive evaluation are described by Rose [21]. Equations for the phase velocity of Rayleigh waves can be derived if we assume the potentials

$$\varphi = A\mathrm{e}^{-k_R q z}\mathrm{e}^{\mathrm{i}k_R(x-c_R t)} \tag{2.23}$$

and

$$\psi = B\mathrm{e}^{-k_R h z}\mathrm{e}^{\mathrm{i}k_R(x-c_R t)}, \tag{2.24}$$

where A and B are arbitrary constants, $q = \sqrt{1-\left(\frac{c_R}{c_L}\right)^2}$, $h = \sqrt{1-\left(\frac{c_R}{c_T}\right)^2}$ and the Rayleigh wave number $k_R = \frac{\omega}{c_R}$ with the Rayleigh wave speed c_R. We can obtain the Rayleigh characteristic equation by applying the stress free boundary conditions and regarding the wave equations (2.15) and (2.16) as

$$\left(2-\frac{c_R^2}{c_T^2}\right)^2 - 4\sqrt{\left(1-\frac{c_R^2}{c_L^2}\right)\left(1-\frac{c_R^2}{c_T^2}\right)} = 0. \tag{2.25}$$

It is noticeable that the frequency does not show up in this equation, which means that the phase velocity of Rayleigh waves is independent of the frequency and the

Rayleigh waves are nondispersive. According to Achenbach [1], The Rayleigh wave speed can be approximated by the equation

$$c_R = \frac{0.862 + 1.14\nu}{1 + \nu} c_T. \tag{2.26}$$

With a common Poisson's ratio of $\nu = 0.3$, this yields an approximate Rayleigh wave speed of $c_R \approx 0.93\, c_T$, so Rayleigh waves are generally slower than both shear waves and longitudinal waves. As described by Graff [6], the particle motion of Rayleigh waves is a combination of longitudinal and shear displacement in a form that results in an elliptical motion, see Figure 2.2. The vertical component of the displacement is about 1.5 times the horizontal component. The motion is retrospect with respect to the direction of wave propagation, i.e. the particles at the free surface move in a counterclockwise rotation for a wave traveling to the right. However, this direction of rotation is reversed in a depth of about 0.192λ. As mentioned before,

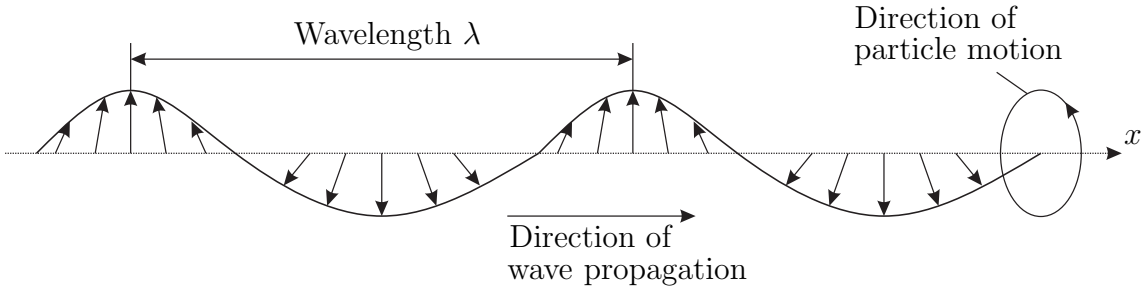

Figure 2.2: particle motion of a Rayleigh wave

the amplitude of Rayleigh waves decays exponentially with depth. According to Achenbach [1], the amplitude and stresses are negligible from a depth of about 1.5λ, so the waves are confined to the surface. This leads to a much smaller dissipation of energy compared to longitudinal and shear waves. Furthermore, as most of the energy is concentrated near the surface, Rayleigh waves are very sensitive to disturbances like cracks, which are normally initiated at the surface. This makes Rayleigh waves a good choice for ultrasonic nondestructive evaluation, but also various other applications like seismology or the detection of landmines [12]. Rayleigh waves are also advantageous

in applications where it is difficult to access the analyzed area because they can follow smoothly curved surfaces [28].

2.3.2 Excitation of Rayleigh Waves

Conventional ultrasonic transducers can generate either longitudinal or shear waves. To generate Rayleigh waves, it is common practice to apply a longitudinal transducer on a wedge-shaped body which is mounted on the specimen in a way that the longitudinal waves impinge the boundary in a certain angle. Due to refraction in the boundary between the wedge and the specimen, Rayleigh waves are generated. To determine the required angle of the incident P-waves, one can write Snell's law (2.22) as

$$c_1 \sin\theta_2 = c_2 \sin\theta_1, \tag{2.27}$$

where c_1 and θ_1 are the wave speed and angle of the incident wave and c_2 and θ_2 are the wave speed and angle of the refracted wave, see Figure 2.3.2. As a Rayleigh wave

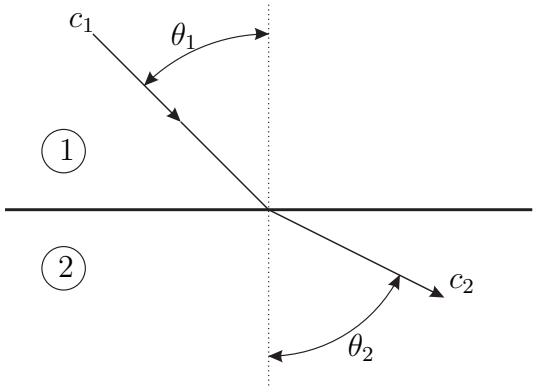

Figure 2.3: Refraction at boundary between wedge and specimen

propagates along the surface, the angle θ_2 is given as $\theta_2 = 90°$ and the Rayleigh wave speed is $c_2 = c_R$. With the longitudinal wave speed $c_1 = c_L$, the required angle of incident can be obtained by

$$\theta_1 = \arcsin\left(\frac{c_L}{c_R}\right). \tag{2.28}$$

As this equation only holds true for $c_L < c_R$, the wedge has to be made of a material with a much slower wave speed than the specimen.

2.4 Nonlinear Wave Propagation

Until now, only linear wave propagation has been considered. However, this was an idealized assumption. In reality, there are generally several phenomena that lead to nonlinear characteristics, i.e. some of the energy of the excited waves will be converted to higher harmonic waves, as depicted in Figure 2.4. This behavior can be useful for ultrasonic nondestructive evaluation. In this section, an overview of one-dimensional nonlinear wave propagation will be given.

The nonlinearity is generated by different causes like inherent lattice anharmonicity,

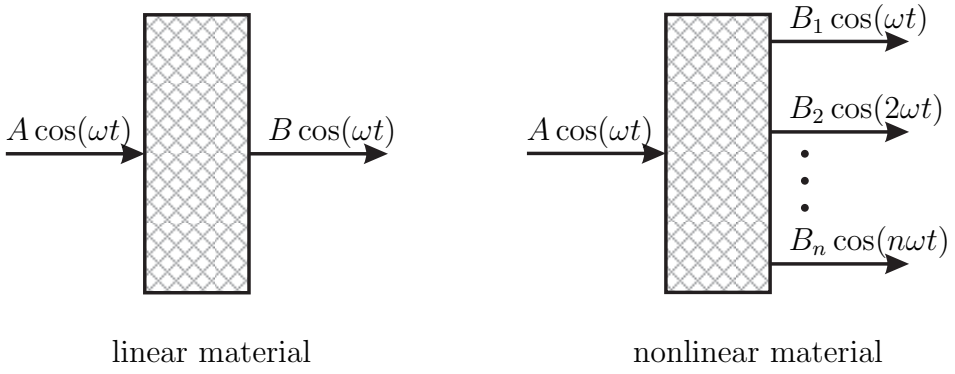

Figure 2.4: Wave propagation in linear and nonlinear material

precipitates, and/or vacancies. Nonlinearity can also be evoked by dislocations or microcracks which are an indicator for material damage. Due to these effects, a sinusoidal wave propagating through the material is distorted as higher harmonics are excited. The degree to which the wave is distorted depends on several factors besides the condition of the material, like fundamental amplitude and fundamental frequency. Within certain boundaries, the amplitude of the higher harmonic wave increases with increasing propagation distance.

2.4.1 Nonlinearity Parameter β

The nonlinearity is generally quantified by the nonlinearity parameter β, for which an expression is derived in this section, following the detailed derivation by Hamilton and Blackstock [7]. The specific strain energy per unit mass W can for small, but not infinitesimal, strains be assumed to have the expansion

$$\rho_0 W = \frac{1}{2} C_{ijkl} E_{ij} E_{kl} + \frac{1}{6} C_{ijklmn} E_{ij} E_{kl} E_{mn} + ..., \tag{2.29}$$

where C_{ijkl} and C_{ijklmn} are the second and third order order elastic constants and

$$E_{ij} = \frac{1}{2} \left(\frac{\partial u_i}{\partial X_j} + \frac{\partial u_j}{\partial X_i} + \frac{\partial u_i}{\partial X_j} \frac{\partial u_j}{\partial X_i} \right) \tag{2.30}$$

is the Lagrangian strain tensor. Introducing the deformation gradient tensor

$$F_{ij} = \frac{\partial x_i}{\partial X_j} \tag{2.31}$$

and the first Piola-Kirchhoff stress tensor, defined to be $P_{ij} = \rho_0 \frac{\partial W}{\partial F_{ij}}$, can be expressed as

$$P_{ij} = C_{ijkl} \frac{\partial u_k}{\partial X_l} + \frac{1}{2} M_{ijklmn} \frac{\partial u_k}{\partial X_l} \frac{\partial u_m}{\partial X_n} + ..., \tag{2.32}$$

where the higher-order coefficients $M_{ijklmn} = C_{ijklmn} + C_{ijln}\delta_{km} + C_{jnkl}\delta_{im} + C_{jlmn}\delta_{ik}$. Now, the equation of motion for finite amplitude waves can be written as

$$P_{ij,j} = \rho_0 \frac{\partial^2 u_i}{\partial t^2}. \tag{2.33}$$

Substituting (2.32) into (2.33) yields

$$\rho_0 \frac{\partial^2 u_i}{\partial t^2} = \frac{\partial^2 u_k}{\partial X_j \partial X_l} \left(C_{ijkl} + M_{ijklmn} \frac{\partial u_m}{\partial X_n} + ... \right). \tag{2.34}$$

For one-dimensional, longitudinal waves, (2.34) is reduced to

$$\frac{\partial^2 u}{\partial t^2} = c_L^2 \frac{\partial^2 u}{\partial X^2} \left(1 - \beta \frac{\partial u}{\partial X} \right) \tag{2.35}$$

with the acoustical nonlinearity parameter

$$\beta = -\left(\frac{3}{2} + \frac{C_{111}}{2\rho_0 c_L^2} \right). \tag{2.36}$$

As most measurement methods measure the amplitude of the displacement, it is desirable to find an expression for β in terms of the harmonic displacement amplitudes A_1 and A_2. Assuming a harmonic excitation of the form $u_0 \sin(\omega t - kx)$, the nonlinear wave equation can be solved as

$$u = u_0 \sin(\omega t - kx) + \frac{\beta}{8} \left(\frac{\omega u_0}{c_L} \right)^2 x \sin(2\omega t - 2kx) u = A_1 \sin(\omega t - kx) + A_2 \sin(2\omega t - 2kx), \tag{2.37}$$

which yields the nonlinearity parameter

$$\beta = \frac{8 c_L^2 A_2}{\omega^2 x A_1^2}. \tag{2.38}$$

It is obvious that the nonlinearity parameter contains only the wave speed, the fundamental frequency, the propagation distance and the fundamental and second harmonic amplitudes, all of which can be easily measured or are constants. This derivation of the nonlinearity parameter is only valid for one-dimensional longitudinal wave propagation. Because of the symmetry of the third order elastic constants, the acoustic nonlinearity of for shear waves vanishes in isotropic materials. As Rayleigh waves are a superposition of longitudinal and shear waves, their nonlinear behavior is comparable to that of longitudinal waves. As shown by Herrmann et al [8], the nonlinear parameter for Rayleigh waves differs from the one for longitudinal waves only by a constant factor, so we can write

$$\beta = \frac{A_2}{\omega^2 x A_1^2} C, \tag{2.39}$$

where the C also contains the wave speeds c_L and c_R and is independent of frequency, as they are constant for a given material.

CHAPTER III

STRESS CORROSION CRACKING

This research focuses on the detection of damage due to stress corrosion cracking. This chapter gives an overview of the mechanism of this particular kind of damage and how the damage was induced under laboratory conditions.

3.1 Mechanism of Stress Corrosion Cracking

Stress Corrosion Cracking (SCC) can pose a great risk to structures like nuclear reactor tubes or fuel pipelines because the cracks generally form late in the life of the structure, but grow very fast. Therefore, it is desirable to detect material damage prior to crack generation. While current methods can mainly detect macrocracks, it has been shown that detection of microcracks in the atomic scale and material discontinuities is possible with nonlinear ultrasonic waves [10], [13], [14]. In this chapter, the damage mechanisms of SCC are explained.

Stress Corrosion Cracking occurs under the combined influence of tensile stress and a mildly corrosive environment. Furthermore, it can occur unexpectedly. R. W. Staehle [23] called the nature of SCC "insidious" for the following reasons: Alloys that are affected by stress corrosion cracking are normally considered passive or non-corroding as they corrode uniformly at very low rates. Similarly, Stress Corrosion Cracking can occur in environmental conditions that are generally considered as being harmless. For example, even the amount of chloride in drinking water can cause cracking of stainless steel when some environmental conditions are met [23]. Under certain electrochemical potential and temperature influences, an iron oxide film forms on the surface of carbon steel. This film protects the underlying material from more corrosion. However, when a sufficiently large tensile stress is applied, the iron oxide film

ruptures in areas of localized plasticity, thereby exposing the underlying bare material to the corrosive environment, see Figure 3.1. At grain boundaries, anodic dissolution leads to crack propagation [9].

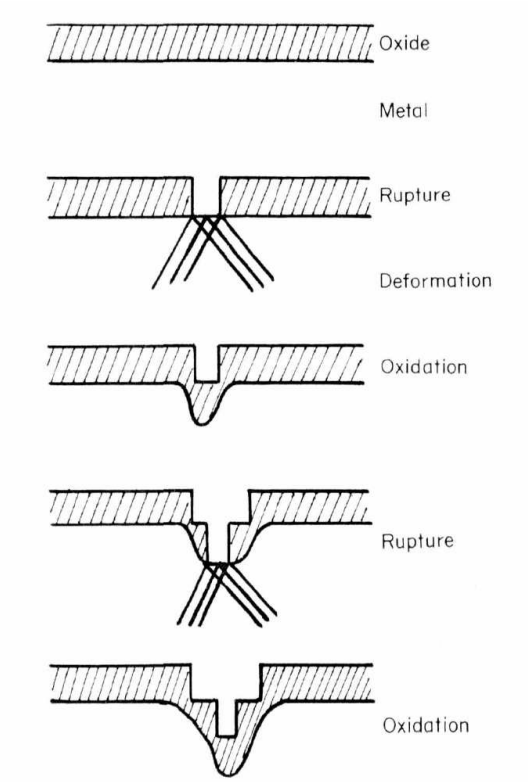

Figure 3.1: Oxide film rupture mechanism, [18]

These microstructural changes lead to an increase in acoustic nonlinearity. First, dislocations, motion, and pileup occur. As shown by Cantrell [2], an increase in dislocation density increases the acoustic nonlinearity. The nonlinearity is then further increased by the formation of microcracks, which cause contact nonlinearity in addition to the nonlinearity caused by dislocations. When the microcracks spread and join each other, macrocracks evolve. These macrocracks cause a large attenuation of particularly the higher harmonic waves, which results in a drop in the nonlinearity parameter. In real-life applications, tensile stresses large enough to cause stress corrosion cracking occur mainly in the vicinity of weld seams which have not been heat-treated. In those areas, the internal stress of the material and the pressure of

the fluid can add up and locally reach or exceed the yield strength of the material.

3.2 Stress Corrosion Cell

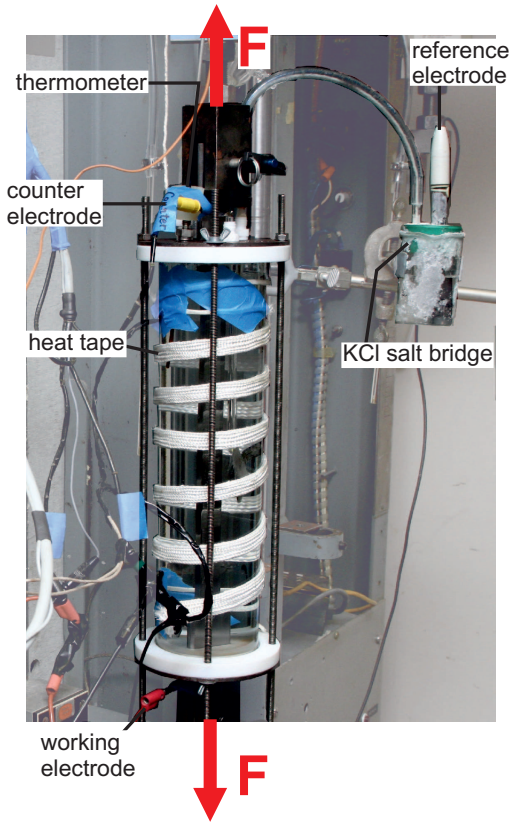

Figure 3.2: Setup of stress corrosion cell

In order to induce SCC damage in the specimens, they are mounted in a stress corrosion cell and exposed to a corrosive environment that has been shown in previous studies to produce stress corrosion cracking [14], [22]. This environment consists of an aqueous solution of 1N sodium carbonate (Na_2CO_3) and 1N sodium bicarbonate ($NaHCO_3$), an electrochemical potential of -650 mV and a temperature of 70°C. A static load varying from nominal yield stress to 10% over nominal yield stress is applied to the specimens over an interval of five days. The corrosion cell itself consists of a glass tube which is closed and sealed at both ends with lids that have cut-outs to allow for the specimen and necessary equipment to be inserted into the solution.

An illustration of the setup can be found in Figure 3.2

To keep the potential constant, a potentiostat Wenking LB75M is used.

3.3 Microscopic Analysis

After importing the damage, the samples are examined with a microscope in order to assess the extent of the damage. Due to superficial corrosion, the surface is covered by an iron oxide layer, whose macroscopic appearance can range from a shiny black film to a matte black cover of iron oxide crystals, which conceals the condition of the material. Therefore, the layer has to be removed by carefully polishing the surface. It is important to remove only enough material to get an unobstructed view of the surface without removing the cracks, i.e. no more than the oxidation layer. An example of a crack can be seen in Figure 3.3.

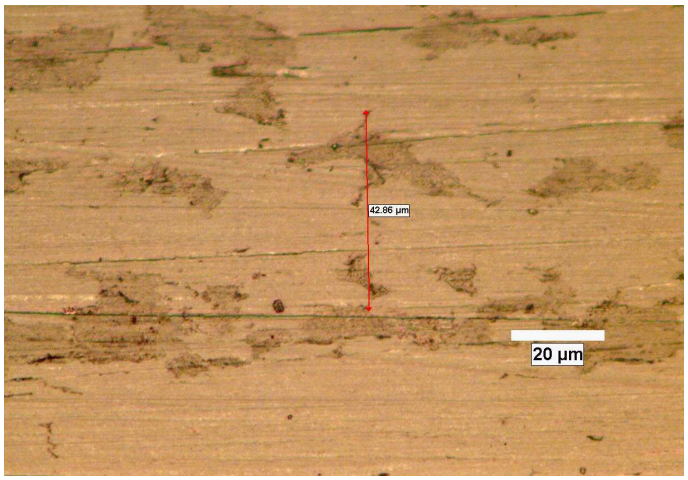

Figure 3.3: Micrograph of polished surface with microcrack

The length of the cracks can be measured easily when the length scale of the microscope for a given magnification factor is known. Measuring the depth of the cracks, however, is more difficult, as it is necessary to cut and polish the specimen in order to get a view of the side of the crack. It is easier to estimate the crack depth on the basis of the empirical aspect ratio that is given as $0.1 < d/l < 0.2$ [22].

Even with careful polishing, it is possible that some iron oxide remains on the surface.

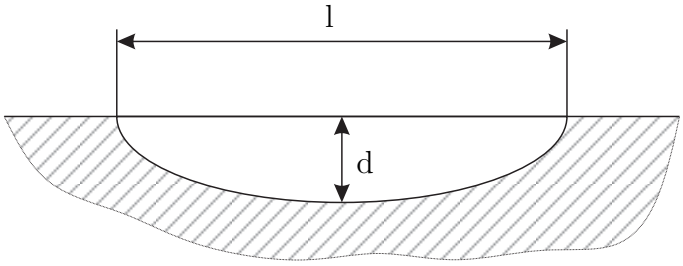

Figure 3.4: Schematical longitudinal cross-section view of a crack

In some cases, it is hard to distinguish between a crack and the border between bare steel and iron oxide. In an attempt to obtain a quantitative value of the extent of the damage, multiple adjoining pictures at the highest available magnification (500x) are taken from a representative area in each specimen, about in the middle of the range of measured propagation distances. In these pictures, the visible cracks are marked, counted, and measured. The length of the area covered by the pictures is about 1.1 mm (this value varies as the pictures overlap), the width is 103 μm. The obtained values for crack density (cracks per mm), average crack length, and range of crack length make it possible to quantify the amount of damage in each specimen. However, as it is not feasible to perform this analysis on large areas of the specimen and due to the above mentioned complexity in reliably identifying cracks, this method contains a large error margin.

CHAPTER IV

SPECIMENS AND MEASUREMENT METHOD

4.1 Specimens

4.1.1 Material

The material used in this research is cold-rolled carbon steel 1018C, which is a common material for buried pipelines for gasoline transport. The chemical composition and nominal mechanical properties are shown in Tables 4.1 and 4.2, respectively.

Table 4.1: Composition of 1018C

Element	C	Mn	Si	S	P
Percentage (%)	0.16	0.78	0.26	0.021	0.005

Table 4.2: Nominal mechanical properties of 1018C

Yield strength (psi)	54000
Tensile strength (psi)	64000

Due to supply issues, not all specimens are manufactured from the same batch of material. Therefore, several mechanical tests have to be performed, as shown later.

4.1.2 Geometry

As the specimens are subjected to tensile stress, it is practical to design them in a dogbone-like shape similar to standard tensile test specimens. In order to be able to perform ultrasonic testing, the test section of the specimens has to be both wide enough to accommodate the wedge transducer and thick enough to allow the Rayleigh surface wave to propagate unimpeded. Under the given circumstances, a width of 0.73" (18.5 mm) and a thickness of 0.2" (5.1 mm) were chosen. The length of the

test section is 10” (254 mm), as shown in Figure 4.1.

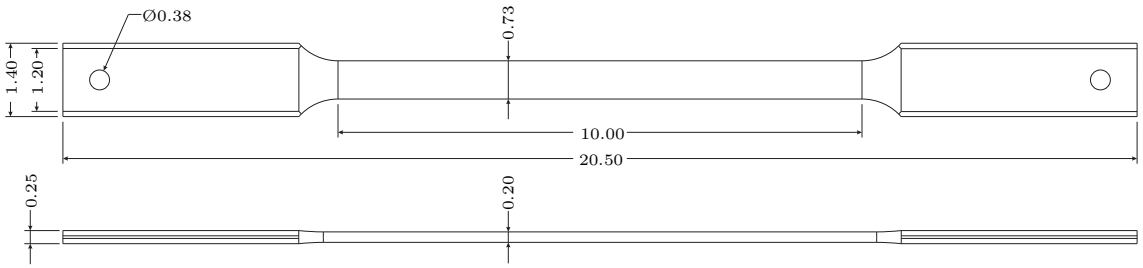

Figure 4.1: drawing of a specimen, all dimensions in inches

The roughly-shaped specimens are cut out of flat bars with a water jet. For specimens 1 through 4, a mill is used for manufacturing the finer shapes. Due to the forces exerted on the material and the consequent bending of the specimen, substantial deviations in the thickness can occur. Therefore, wire EDM is used for later specimens. This technique allows for much finer tolerances. As Rayleigh surface waves are very sensitive to surface roughness and therefore require a very smooth surface, the surfaces of the test section are then sanded and polished manually to obtain a surface as shown in Figure 4.2. Possible variances in the cross-section area due to manufacturing tolerances and subsequent polishing have to be accounted for when calculating the tensile force.

Figure 4.2: Undamaged specimen

4.2 Ultrasonic Measurement

Of many different methods to generate Rayleigh surface waves, the wedge method is one of the most common ones. As this technique is proven and the required equipment is easily available, it is used in this research. The principle of the wedge method is based upon the mode conversion from longitudinal waves to Rayleigh waves in the

contact area of two bodies. The following sections give an overview of the equipment used in this research.

4.2.1 Wedges

The theoretical background for the excitation of Rayleigh waves can be found in Section 2.3.2. As shown in Equation (2.28), the longitudinal wave speed of the wedge material has to be smaller than the Rayleigh wave speed of the material of the specimen. Using Equation (2.26), a Poisson's ratio of $\nu = 0.3$, and a transverse wave speed of $3200m/s$ for steel [1], we obtain the Rayleigh wave speed $c_R \approx 2964m/s$. With a longitudinal wave speed of $c_L = 2720m/s$, plexiglass fulfills the condition $c_L/c_R < 1$ and is therefore used as a wedge material. With these values, the required wedge angle is $\theta_1 \approx 66.6°$. Figure 4.3 shows a wedge with attached transducer. The same type of wedge is used for both transmitting and receiving transducers.

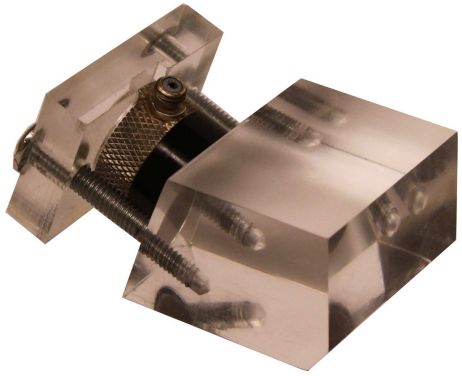

Figure 4.3: Plexiglass wedge with attached transducer

4.2.2 Transducers

The transducers used in this research are piezoelectric longitudinal wave transducers. As it is crucial for nonlinear ultrasonic measurements to measure the second harmonic amplitude, the center frequency of the receiving transducer ia chosen to be about twice as high as the fundamental frequency. The receiving transducer is a narrowband transducer, but its bandwidth is still wide enough to detect the fundamental

signal with sufficient sensitivity. Table 4.3 provides detailed information about the transducers used. The transmitting transducer was built on request as most standard

Table 4.3: Specification of transducers

	Model	Type	center frequency	diameter
Transmitter	Panametrics X1055	Custom made	2.25 Mhz	0.5”
Receiver	Panametrics A109S	Narrowband	5 Mhz	0.5”

transducers can be damaged by the high input voltage needed to excite a wave with a sufficiently large amplitude.

It has to be noted that piezoelectric transducers have a certain inherent nonlinearity. However, since the input frequency and amplitude are kept constant and only the propagation distance as varied, the effect of this nonlinearity can be avoided.

4.2.3 Amplifier

As shown in Section 2.4.1, the second harmonic amplitude is proportional to the square of the fundamental amplitude. In order to be able to reliably measure the second harmonic amplitude in relation to the fundamental amplitude and noise, it is therefore necessary to maximize the fundamental amplitude by means of amplifying the input signal. To achieve a sufficiently high amplitude of the fundamental wave, a high-power gated amplifier (RITEC RAM-5000 MARK IV) is used. Table 4.4 shows some specifications of this amplifier. Another advantage of the RITEC RAM-5000 is the fact that it produces a very clean sinusoidal signal with only a small inherent nonlinearity.

Table 4.4: Technical data of RITEC RAM-5000

Frequency Range for Synthesizer	50 kHz to 22 Mhz
Nominal Frequency Range for Gated Amplifier	250 kHz to 17.5 Mhz
On/Off Ratio for Gated Amplifier	$>$ 140 dB
Typical RMS Output Power	1.5 kW between 0.25 and 7Mhz

For all measurements, the same signal is used. The transmitter is excited with a tone

burst of a frequency of 2.25 Mhz, which is the center frequency of the transmitter, and a burst width of 25 cycles, which produces a large enough steady-state portion of the signal. The output level is set to 90% of the maximum capacity to provide for a sufficiently large amplitude. Furthermore, it has been shown in previous work that on low output settings, the signal generated by the RITEC system is more distorted than on high output settings. [26] The frequency of 2.25 Mhz leads to a wavelength of

$$\lambda = \frac{c_R}{f} = \frac{2964\ m/s}{2.25 \times 10^6\ 1/s} \approx 1.32\ mm. \tag{4.1}$$

As almost all the energy of Rayleigh waves is concentrated in a depth of less than 1.5λ (see Section 2.3.1), the thickness of 5.1mm is sufficiently large that no significant displacement occurs on the opposite surface which would otherwise create reflections that can generate Lamb type waves. Therefore, it can be assumed that the wave in this plate indeed has the character of a Rayleigh wave.

4.2.4 Oscilloscope

The signals are recorded with a Tektronix TDS 420 Oscilloscope at a sampling rate of 100 MHz and averaged over 507 measurements to maximize the signal to noise ratio.

4.2.5 Experimental Setup and Procedure

As described above, the input frequency and amplitude are kept constant for every measurement. In order to determine the nonlinearity parameter β, the propagation distance x is varied. For every measurement, the procedure is the same. First, the specimen is clamped to a stand and carefully aligned to a ruler, which acts as a guide for the wedges. The distance between the ruler and the specimen is such that the center lines of the wedges and the specimen are coincident. This ensures an optimal transmission of the waves, as even a small misalignment can significantly distort the measured values, as shown by Walker [26]. Furthermore, the ruler is used to measure the propagation distance. The transducers are fixed to the wedges with screws.

To ensure a good transmission of the waves from the transducer to the wedge, light lubrication oil is used as a couplant. Then, the transmitter wedge is clamped onto the specimen, carefully aligned with the aforementioned ruler. Between the wedge and the specimen, the same couplant as before is used. It is important to wipe away any excess couplant oil on the surface of the specimen, as it can significantly increase attenuation. After that, the wedge is given 30 minutes to settle as tests have shown that in the first 30 minutes after application of the wedge, the transmission characteristic changes over time [26]. Likewise, the RITEC system has to be turned on 30 minutes before starting the measurements in order to warm up.

After the 30 minutes, the receiver wedge is applied in the same way as the transmitter wedge. As the receiver wedge is reapplied multiple times during one set of measurements in order to vary the propagation distance, it would not be feasible to wait for 30 minutes each time. However, as the interval between the application of the receiver wedge and the measurement is the same for each measurement, the influence of the settling is considered constant. The transmitter wedge, on the other hand, is fixed to the specimen for the duration of the whole set of measurements. A schematic illustration of the setup is shown in Figure 4.4.

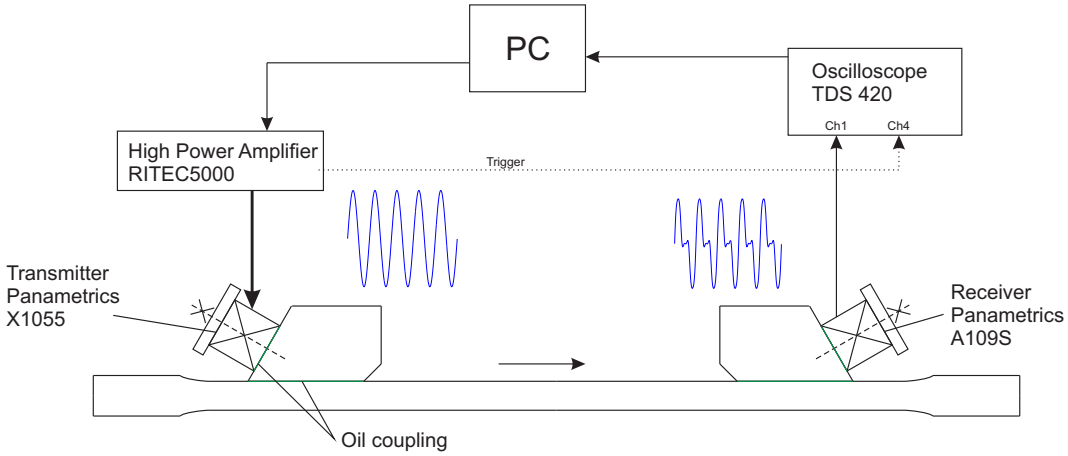

Figure 4.4: Setup for ultrasonic measurements

The signal is generated and recorded as described in Sections 4.2.3 and 4.2.4. The

signal recorded by the oscilloscope is then saved in an Excel file for further signal processing. Afterwards, the receiver wedge is removed from the specimen, any residual couplant oil is removed and the wedge is reapplied in the same way as before at a different position. The measurements are conducted at propagation distances from 50 to 140 mm in increments of 5 mm, which results in 19 data points per set of measurements.

As there are many factors which can evoke inconsistencies between the individual measurements, five sets of measurements, each consisting of 19 data points, are conducted for each sample and each material condition.

4.2.6 Signal Processing

The first and last few cycles of each sine-burst are transient, i.e. the signal is not a clear sine wave. Therefore, those parts are not used for the following signal processing; only the steady-state portion is used, see Figure 4.5. Afterwards, a Hann-window is

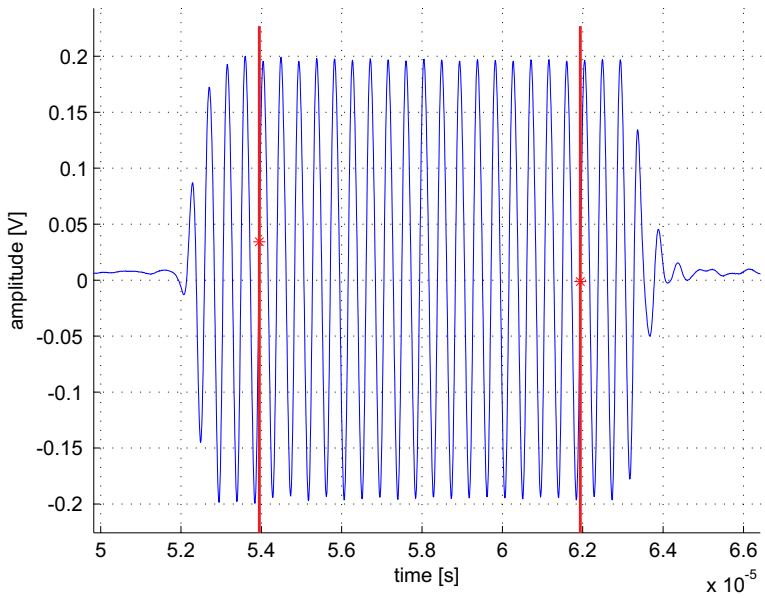

Figure 4.5: Recieved signal with steady-state portion marked by red lines

applied to the steady-state portion, see Figure 4.6. The Hann-window is applied because the next step in processing the signal involves a Fourier transform. Using

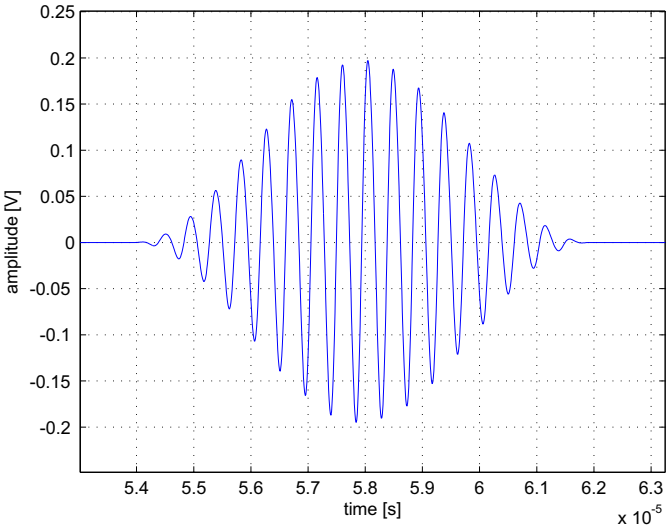

Figure 4.6: Signal with applied Hann-window

only a rectangular window to isolate the steady-state portion would result in a much less clear frequency spectrum. The Hann-window minimizes the amplitudes of the side lobes [17]. Figure 4.7 shows the frequency spectrum of the same signal, one with a rectangular window and the other with a Hann-window. This evaluation is done for

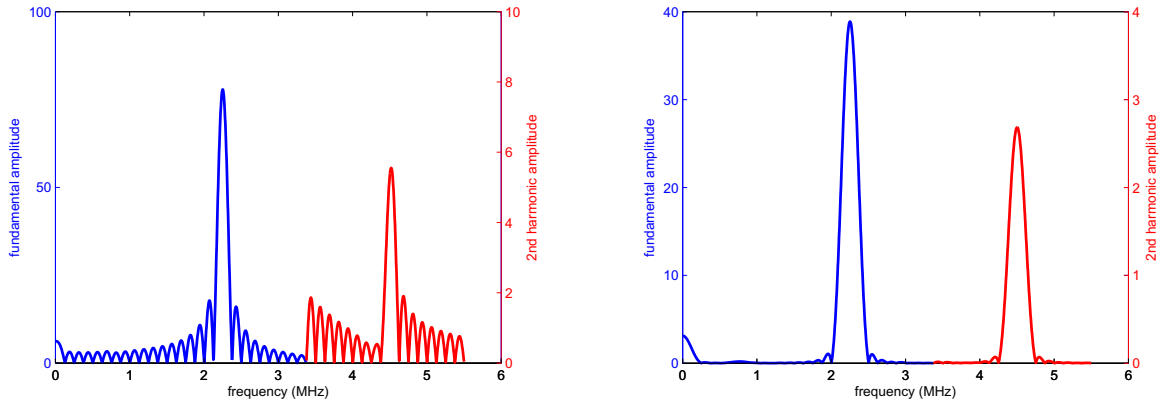

Figure 4.7: Frequency spectrum for signal with rectangular window (left) and Hann-window (right)

each propagation distance. Afterwards, the normalized second harmonic amplitude A_2/A_1^2 can be plotted versus the propagation distance x as shown in Figure 4.8. One can see that for small propagation distances, the normalized second harmonic

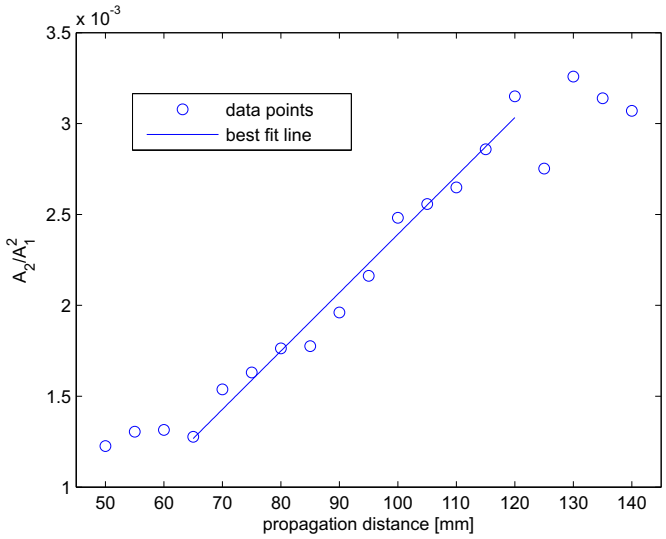

Figure 4.8: Cumulative nonlinearity of a single measurement set

amplitude is more or less constant. This is due to near field effects. In this region, the wave has not yet fully developed. Calculating the extent of the near field is a non-trivial problem as this phenomenon is not yet fully explored. There are several different formulas to estimate the extent of the near field. One of them is given in [11]:

$$\frac{r_{min}}{L} \approx \frac{L}{4\lambda}, \tag{4.2}$$

where r_{min} marks the beginning of the far field, L is the greatest dimension of the source, and λ is the wavelength. In this case, the diameter of the transducer is $L = 12.7$ mm, the fundamental wavelength is $\lambda_1 = 1.32$ mm (see Equation (4.1)), and the wavelength of the second harmonic is $\lambda_2 = \frac{1}{2}\lambda_1 = 0.66$ mm. This leads to an estimated length of the near field of $r_{min,1} \approx \frac{12.7^2}{4 \cdot 1.32} = 30.5$ mm for the fundamental wave and $r_{min,2} \approx \frac{12.7^2}{4 \cdot 0.66} = 61$ mm for the second harmonic wave. This seems to be consistent with the observations made in Figure 4.8. For larger propagation distances, the normalized second harmonic amplitude reaches a saturation and does not further increase. This is partly due to scattering or reflections of the wave at the side surfaces of the sample which distort the wave, and partly due to in increasing

influence of attenuation. As higher frequency waves have a higher attenuation than lower frequency waves, the second harmonic amplitude decreases faster than to the fundamental amplitude for large propagation distances. Figure 4.9 shows a comparison between the fundamental amplitude and the second harmonic amplitude. One can clearly see the effect of higher attenuation of the second harmonic at propagation distances of 115 mm and above.

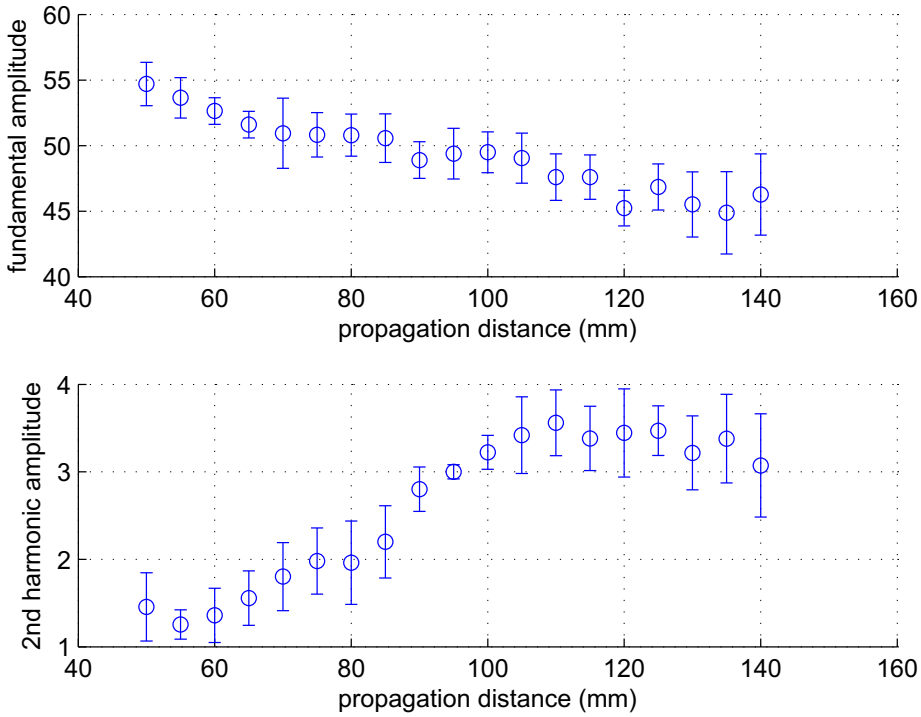

Figure 4.9: Fundamental and second harmonic amplitudes in undamaged specimen 2

In the middle part, however, there is an approximately linear relationship between the ratio normalized second harmonic amplitude and the propagation distance x. According to Equation (2.39), the slope of the best fit line, which can be expressed as $\frac{A_2 x}{A_1^2}$, is directly proportional to the nonlinearity parameter β.

However, it is not always easy to determine the exact boundaries of the approximately linear interval. In some cases, the range of the near field varies between different

specimen. Even more common is a variation of the saturation limit. Therefore, the evaluation interval has to be chosen individually for each specimen. For most specimens, an evaluation interval from 60 to 120 mm is appropriate, but in some cases the interval has to be altered. Choosing different evaluation intervals can cause considerable deviations in the obtained nonlinearity parameter. Because deciding about the boundaries of the interval is somewhat subjective, the results are in danger of being distorted.

4.3 Repeatability and Accuracy of Measurements

As described in Section 4.2.5, several factors have to be taken account for in order to provide the same conditions for each measurement when applying the wedges, e.g. the amount of couplant oil used, the alignment of the wedges, and thorough removal of excess couplant oil. Nevertheless, even when the highest amount of attention is

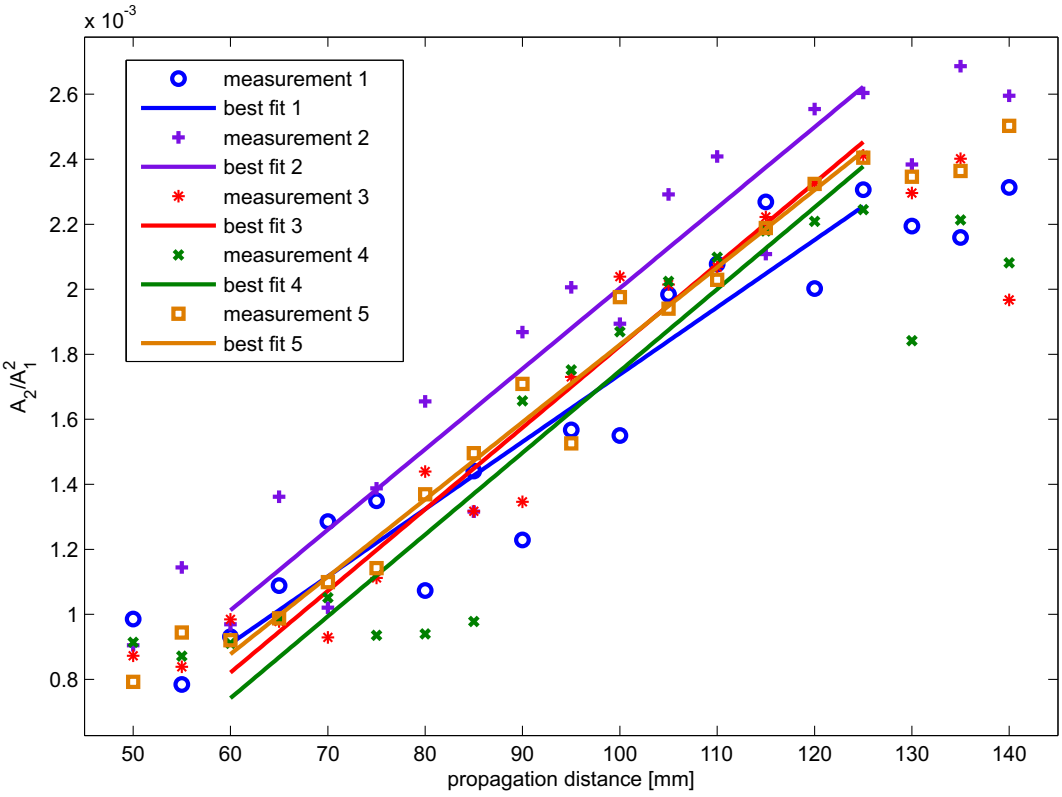

Figure 4.10: Comparison between five measurements of damaged specimen 3

paid to these factors, significant deviations between several measurements at the same point can occur. The results of five sets of measurements of the same specimen are shown in Figure 4.10. Even though individual data points show large deviations from the correspondent data points from other measurements, the resultant best-fit lines have little deviation from each other both in absolute values and slopes. In this particular example, the highest deviation of the slope between one measurement set (here measurement 1) and the averaged result (see Figure 5.7) is 13.4%. In order to minimize the influence of those deviations, the averaged values from five individual measurements are used for the subsequent evaluation. For this case, this leads to a standard deviation of the obtained results of 7.0%. So we can assume that the deviation and systematic error of the measurement procedure used is about 7%

4.4 Tensile tests

The material specifications of steel only dictate minimum values for yield strength. Often, the actual yield strength of a material is higher than the required minimum strength. Therefore, tensile tests are performed to determine the actual yield strength. As mentioned earlier, not all specimens are made from steel of the same batch, therefore multiple tensile tests are performed. However, the differences in yield strength between the different batches are received only after some SCC tests were already performed. Batches 1 and 2 are obtained from the same supplier, while the steel from batch 3 is obtained from a different supplier.

4.4.1 Batch 2

As the supply of steel of batch 2 is limited, there is no undamaged specimen available. Therefore, specimen 3 is reused for this test. This specimen is chosen because microscopic and ultrasonic analysis show only minimal damage. Prior to the tensile test, the surface is ground in order to remove any superficial damage due to corrosion. With a maximum measured crack length of 41 μm (see Section 5.2.3), the maximum

crack depth can be estimated as $d_{\max} \approx 0.2 \cdot l_{\max} = 0.2 \cdot 41\ \mu\text{m} \approx 8\ \mu\text{m}$. On each surface, at least 25 μm are ground off, ensuring reliable removal of all cracks. The conducted tensile test (see Figure 4.11) reveals that the material has no pronounced yield point, but a rather brittle behavior. The ultimate tensile strength is 94.2 ksi.

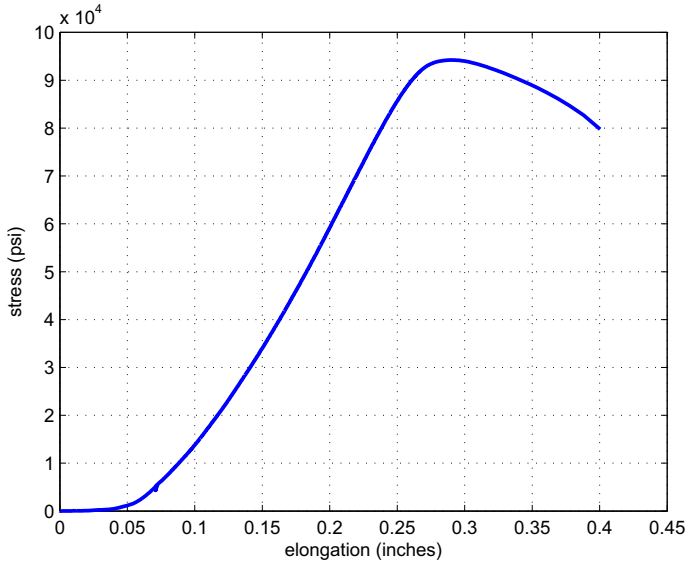

Figure 4.11: Tensile test of batch 2 steel. The flat section in the beginning is caused by slip at the grips

This behavior makes it hard to induce large amounts of strain into the specimens, as they do not yield. However, as shown in Chapter 5, the strain due to elastic elongation is sufficiently large to initiate stress corrosion cracking. As no pronounced yield point exists, the applied stress in the tests is specified in multiples of nominal yield stress.

4.4.2 Batch 3

A tensile test with batch 3 material is performed using a regular specimen. The resultant stress-strain curve is shown in Figure 4.12. As shown in Figure 4.13, the actual yield strength is 54.0 ksi, which is exactly the nominal value. The ultimate tensile strength is 69.3 ksi.

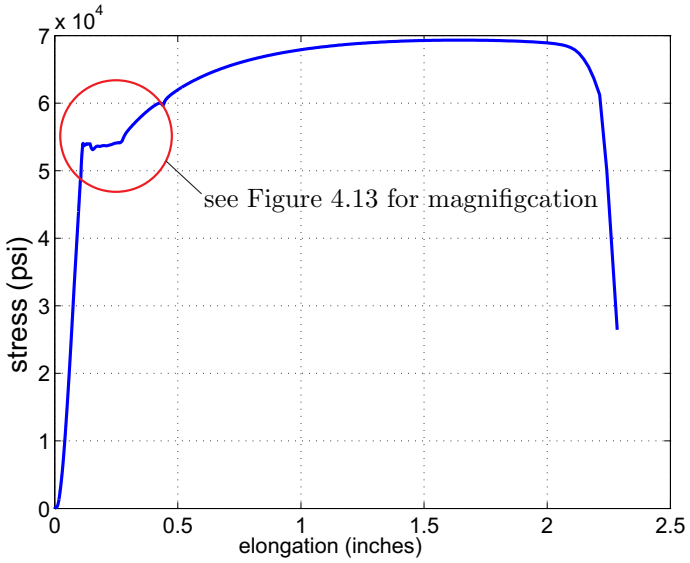

Figure 4.12: Tensile test of batch 3 steel

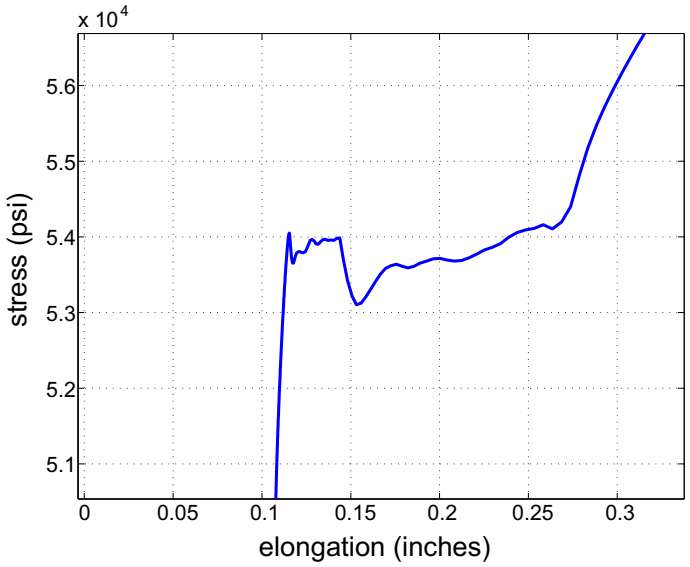

Figure 4.13: Tensile test of batch 3 steel, magnification

4.5 Microhardness Tests

In addition to the tensile tests, microhardness tests using the Vickers method are performed. In the grip sections of one specimen of each batch of steel, the Vickers hardness is determined by averaging the results of five individual tests. The testing parameters are kept constant at a load of 1 kgf (9.81 N) and a loading time of 5 s. The results of the hardness test can be found in Table 4.5. The hardness of batches

Table 4.5: Hardness of the tested material

Batch #	tested hardness (in HV 1/5)
1	231
2	236
3	175

1 and 2 are almost the same, while batch 3 is a lot softer. On the basis of the hardness, an approximation of the strength of the materials can be determined, as an approximately linear relationship between hardness and ultimate tensile strength exists [20]. However, sources specify different values for the factor which refers the tensile strength to the hardness. Furthermore, they use different units. Therefore, such a factor is determined with the results of the previous tests in the units used earlier, i.e. stress in ksi and hardness in HV 1/5. The obtained factor shall be called z, with $z = \sigma_{ult}/HV$. For batch 2, the factor $z_2 = 94.2/236 = 0.399$ is obtained. For batch 3, the factor is $z_3 = 69.3/175 = 0.396$. These values are very close, so a linear relationship can indeed be assumed. In the following, the approximate factor $z = \frac{z_2+z_3}{2} \approx 0.398$ shall be used. With this factor, an approximate value for the ultimate tensile strength of batch 1 can be obtained as $\sigma_{ult1} = HV_1 \cdot z \approx 91.9ksi$. Because of the fact that batches 1 and 2 are purchased from the same supplier and because the specimens made from those two batches show a similar strain behavior when subjected to stress in the stress corrosion cell, it can be safely assumed that the nominal yield stress of 54 ksi is well within the area of pure elastic behavior of batch 1 as well. Therefore, an additional tensile test for batch 1 is not deemed necessary.

CHAPTER V

RESULTS

In this chapter, the results of the ultrasonic measurements and microscopic analysis are discussed. First, the results for each individual specimen are presented, then the results are compared.

5.1 Preliminary tests

As mentioned in Section 4.1.1, material from different batches has to be used for certain samples. Therefore, multiple tensile test are performed to determine the actual yield strength of the individual samples. For the Stress Corrosion Cracking, however, the applied load is specified in multiples of the nominal yield stress.

5.2 Individual Specimens

In this section, the results of the individual specimens are presented. An overview of the material and test parameters is given in Table 5.1.

Table 5.1: Material and test parameters of the individual samples.

Specimen #	Batch #	tensile stress (in multiples of nominal yield strength)
1	1	1.00
2	2	1.078
3	2	1.10
4	2	1.10
5	3	1.00

5.2.1 Specimen 1

5.2.1.1 SSC and microscopy

Specimen 1 is held at nominal yield stress for 5 days. After the corrosion, the surface is shiny black in the area which was near the platinum electrode during the corrosion, and slightly matte black in areas which were farther away from the electrode. After careful polishing, some cracks are visible in both areas. Closer inspection as described in Section 3.3, namely counting and measuring the visible cracks on 10 micrographs of the surface, yields an average crack density of 8.5 cracks per mm. The crack length in the inspected area ranges from 20 to 65 μm with an average crack length of 34 μm. An exemplary microscopic image of the surface with a crack is shown in Figure 5.1.

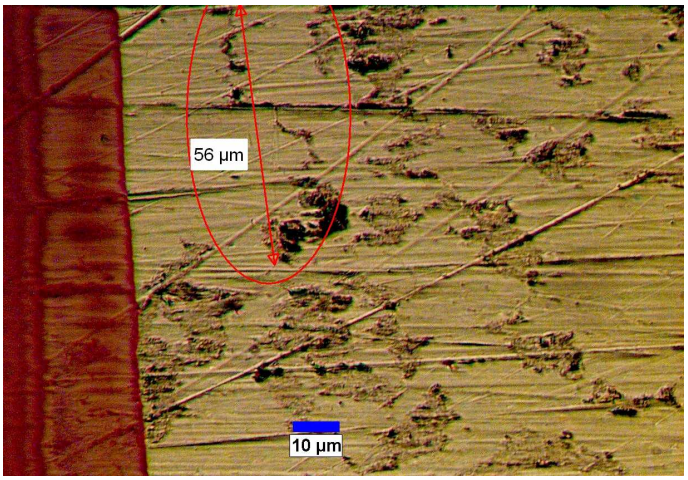

Figure 5.1: Microscopic image of damaged specimen # 1, 500x magnification

5.2.1.2 Ultrasonic Measurement

Figure 5.2 shows the measured nonlinearity of specimen 1 in both the undamaged and damaged conditions. The slope of the best fit line of the damaged specimen is 18.9% higher than that of the undamaged specimen, which is an indicator of a noticeable increase in nonlinearity.

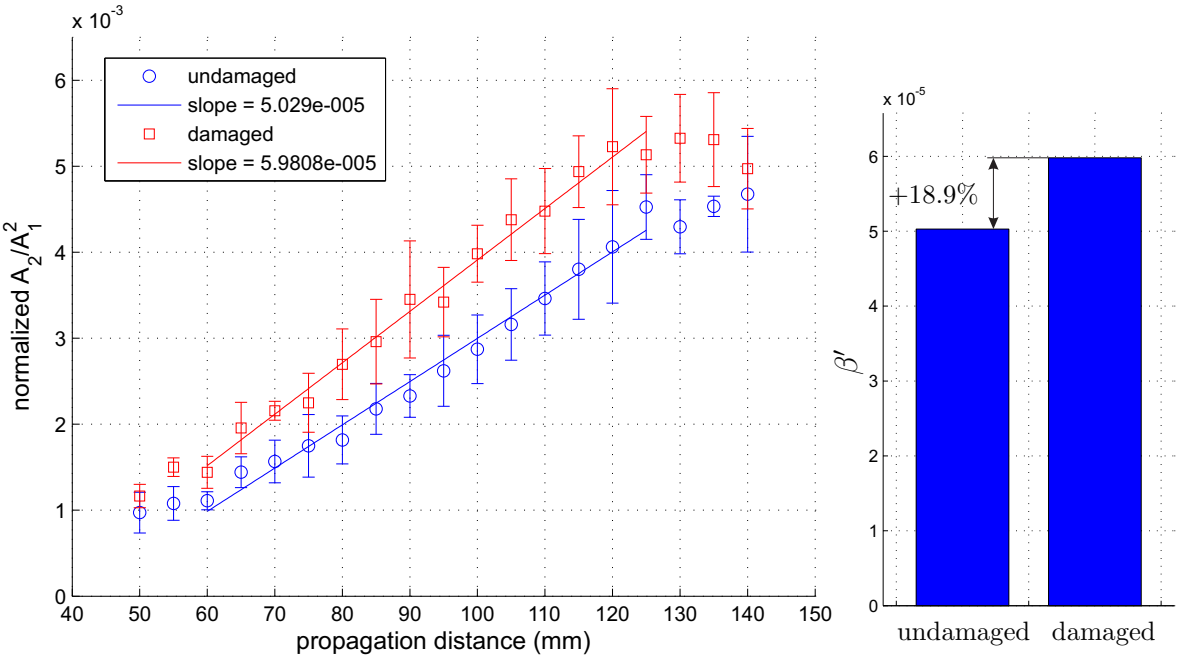

Figure 5.2: Comparison of nonlinearity of undamaged and damaged specimen # 1

5.2.2 Specimen 2

5.2.2.1 SSC and microscopy

Specimen 2 is held at 7.8% over nominal yield stress. After the corrosion, the surface is mostly covered by iron oxide crystals. After polishing the surface, more cracks than in specimen 1 are visible. Furthermore, there seems to be some pitting which is visible in Figure 5.3. Counting the cracks on micrographs as described before yields

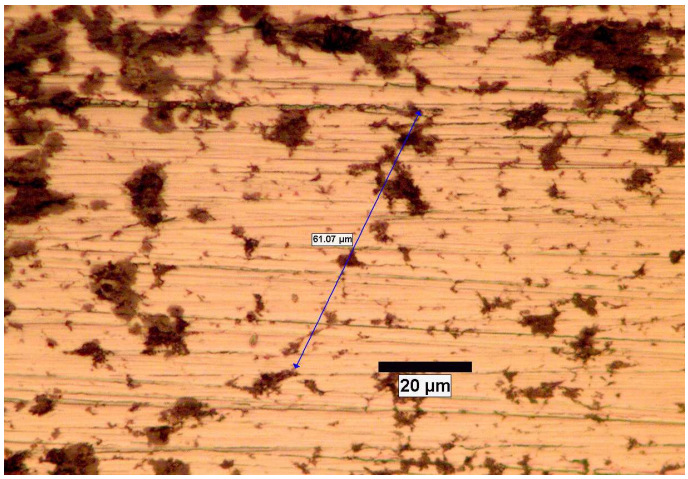

Figure 5.3: Microscopic image of damaged specimen # 2, 500x magnification

an average crack density of 12.5 cracks per mm. The length of the cracks ranges from 19 to 83 μm, with an average crack length of 48.1 μm.

5.2.2.2 Ultrasonic Measurement

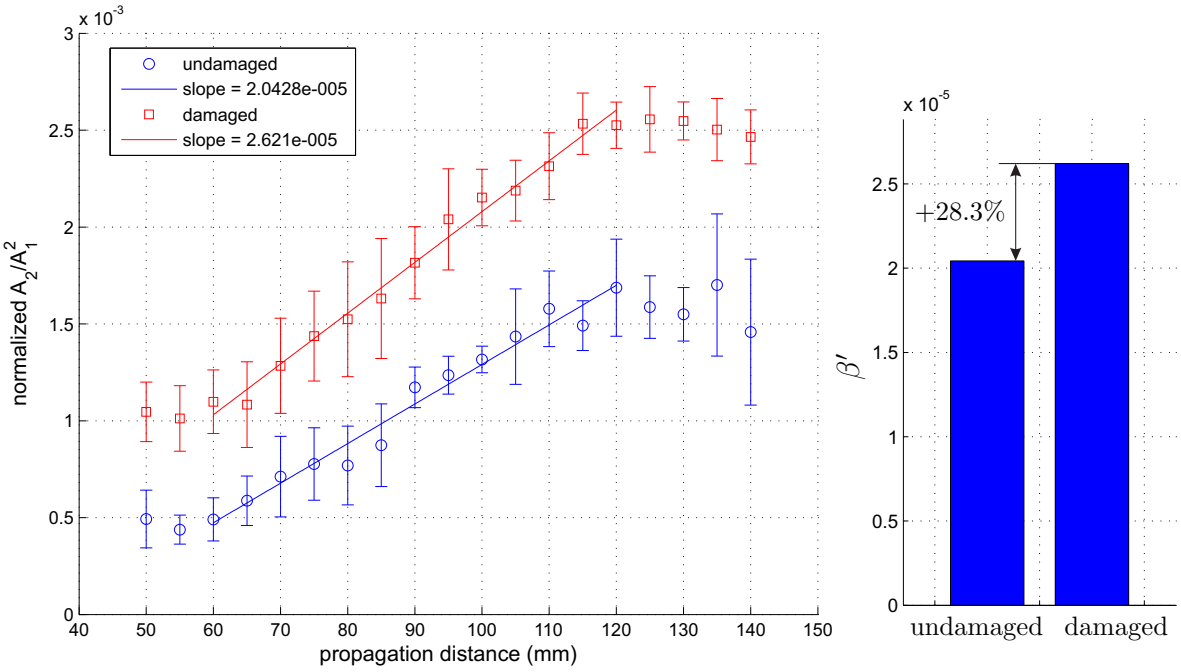

Figure 5.4: Comparison of nonlinearity of undamaged and damaged specimen # 2

Figure 5.4 shows the measured nonlinearity of specimen 2 both in the undamaged and damaged conditions. The slope of the best fit line of the damaged specimen is 28.3% higher than that of the undamaged specimen. This increase in the nonlinearity parameter coincides with the increased density and length of cracks compared to specimen 1. There is also a considerable offset in the nonlinearity parameter which might be caused by different transmission conditions between the wedge and the specimen.

5.2.3 Specimen 3

5.2.3.1 SCC and microscopy

Specimen 3 is held at 10% over nominal yield stress. However, during the corrosion process, the potentiostat fails. Therefore, the applied electrochemical potential could not be kept constant. After the corrosion, the whole surface is covered by iron oxide crystals. This makes the surface macroscopically look matte black. Under the microscope, the crystals become visible, as shown in Figure 5.5. The surface is also

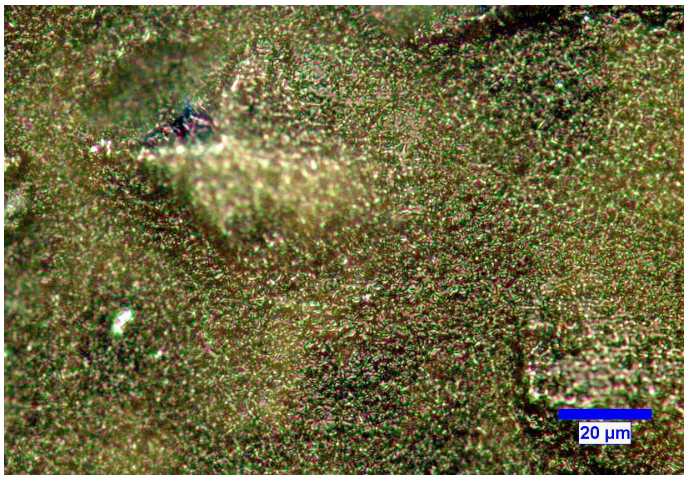

Figure 5.5: Microscopic image of damaged specimen # 3, 500x magnification

noticeably uneven. There are many areas with agglomerations of iron oxide. In Figure 5.5, out-of-focus (unsharp) areas indicate areas of a different height. After polishing, some small cracks are visible on the surface, see Figure 5.6. Closer inspection yields an average crack density of 14.1 cracks per mm. The length of the cracks ranges from 10 to 41 μm, with an average crack length of 20.9 μm. There are also darker areas on the surface which indicate pitting.

5.2.3.2 Ultrasonic Measurement

Figure 5.7 shows the measured nonlinearity of specimen 3 in both the undamaged and damaged conditions. The slope of the best fit line of the damaged specimen is 1.3% higher than that of the undamaged specimen. The best fit lines of the undamaged

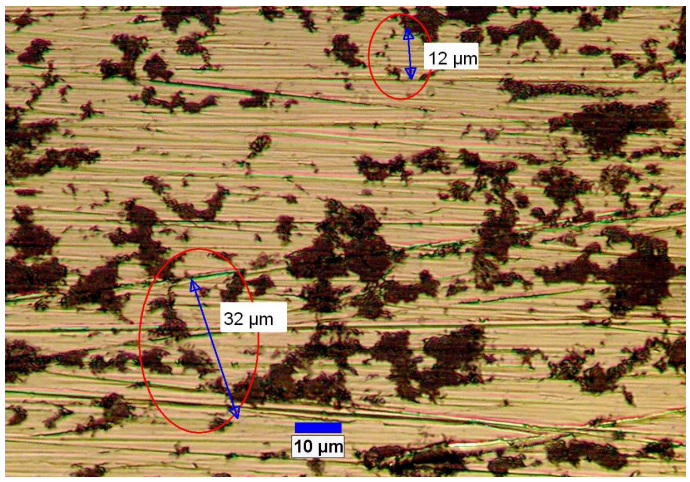

Figure 5.6: Microscopic image of damaged specimen # 3, 500x magnification

and damaged specimen are almost identical (within the measuring accuracy). This behavior is interesting. On the one hand, it was discovered that the environmental

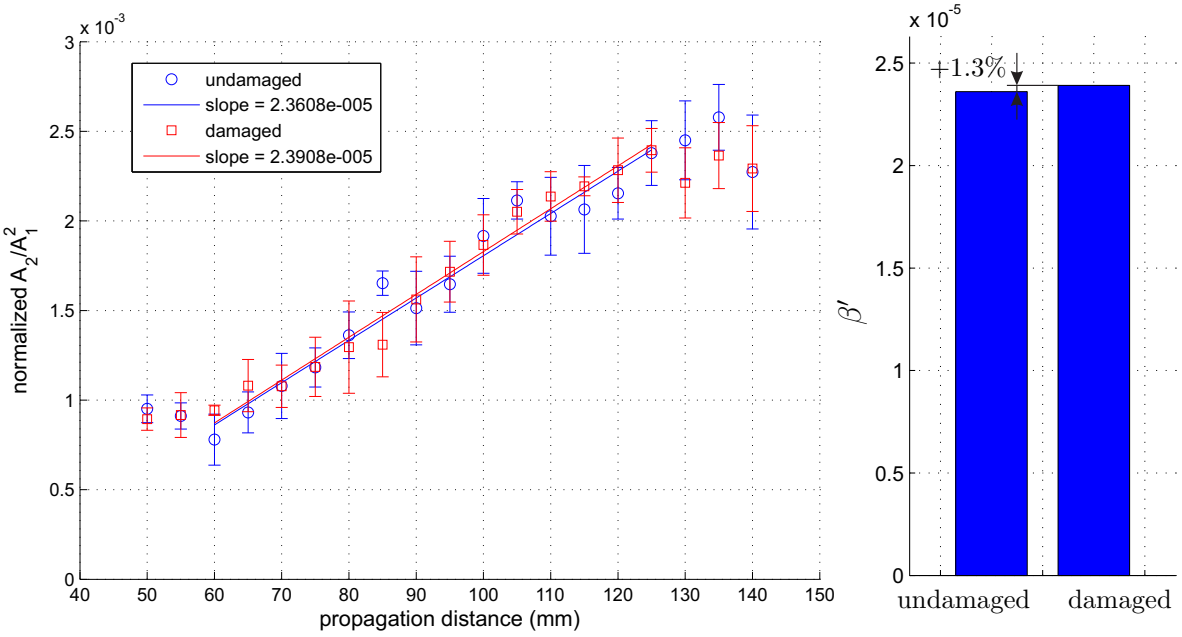

Figure 5.7: Comparison of nonlinearity of undamaged and damaged specimen # 3

conditions for stress corrosion cracking were not given during the corrosion phase. Considering this fact, the obtained results look reasonable. On the other hand, the microscopy revealed a considerable number of cracks. However, these cracks are very small compared to those found on specimens 1 and 2. The small size of the cracks

can be an indicator of very weak stress corrosion cracking. It is also noteworthy that there is no offset in the nonlinearity factor between the undamaged and the damaged specimen.

5.2.4 Specimen 4

5.2.4.1 SCC and microscopy

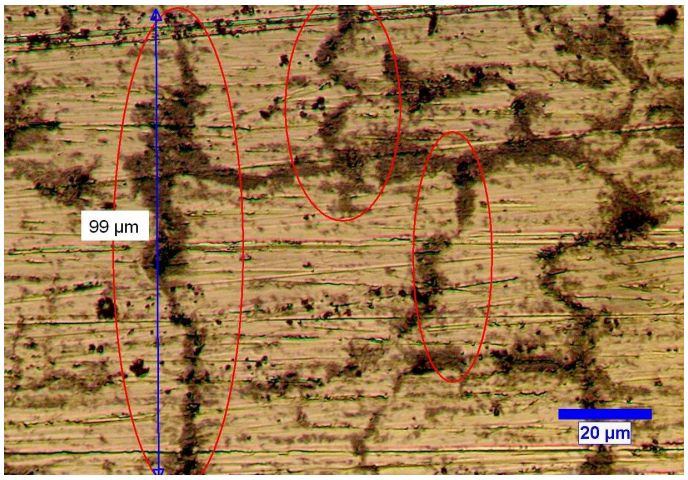

Figure 5.8: Microscopic image of damaged specimen # 4, 500x magnification

Due to the potentiostat failure during the corrosion of specimen 3, this test is repeated with specimen 4, so the same test parameters are used for specimen 4. The replacement potentiostat (which is of the same type as the one previously used) functions well and is able to keep the applied potential constant. Furthermore, a larger platinum electrode is used. Due to the last fact, the most part of the surface is covered in a shiny black iron oxide film instead of crystals after the corrosion. The surface shows a lot more cracks than the previous specimens. The average crack density is 22.6 cracks per mm. The crack length ranges from 20 to 99 μm, with an average crack length of 44.9 μm. Figure 5.8 shows a micrograph of the damaged specimen 4; multiple cracks are visible. At the edges of the cracks, there are still iron oxide residues which can not be removed without removing the cracks as well.

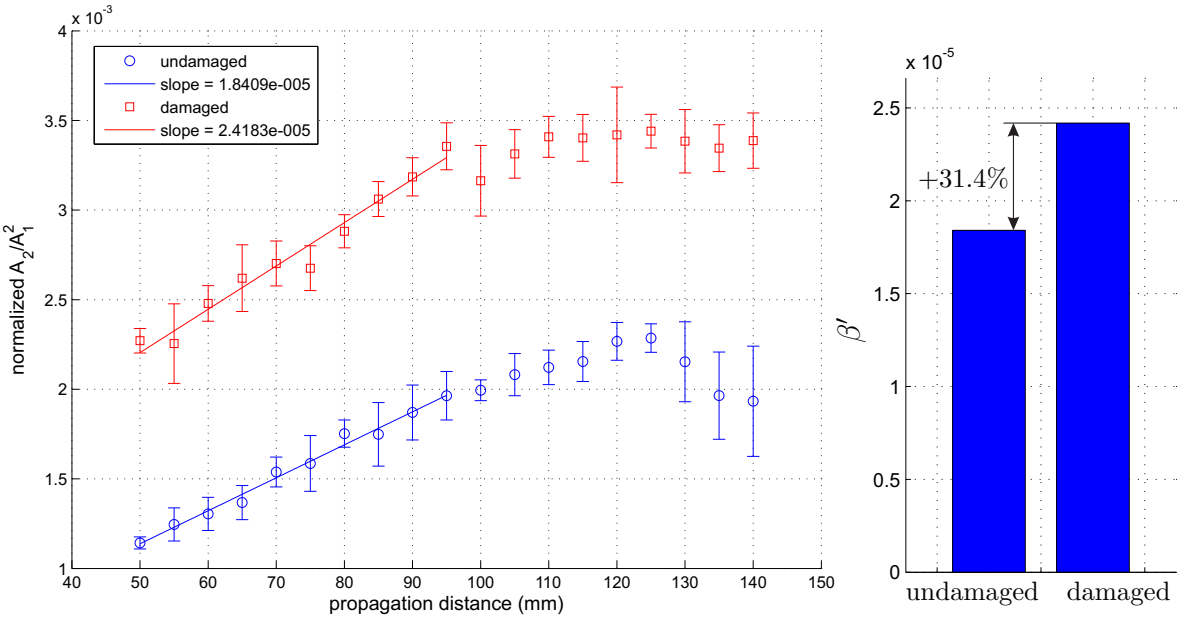

Figure 5.9: Comparison of nonlinearity of undamaged and damaged specimen # 4

5.2.4.2 Ultrasonic Measurement

Figure 5.9 shows the measured nonlinearity of specimen 4 in both the undamaged and damaged conditions. The slope of the best fit line of the damaged specimen is 31.4% higher than that of the undamaged specimen. Some facts are noticeable: First of all, there is a large offset in the nonlinearity between the undamaged and the damaged states, which can be explained by different transmission conditions between the wedge and the specimen. Secondly, there is a bend in the data points of the undamaged specimen at a propagation distance between 95 and 100 mm. In the damaged specimen, there is a sharp drop in nonlinearity at the same position. Even though microscopy did not reveal any anomalies, the data suggests a preexistent condition in the material. Therefore, the best fit line is only calculated using data up to the 10^{th} datapoint (95 mm). On the other hand, no considerable near field effect is visible. Therefore, the first data point are also included in the calculation of the best fit line. It has to be noted that choosing different intervals for calculating the best fit line can alter the obtained results strongly.

5.2.5 Specimen 5

As shown in Section 4.4, the yield strength of the material used for specimen 5 is much lower than that of the other specimens. Therefore, The SCC test is performed again with a stress of 54 ksi, which is the nominal yield strength and also the actual yield strength of specimen 5. Consequently, the elongation experienced by specimen 5 is larger than that of the previous specimens, as it actually yields.

5.2.5.1 SCC and microscopy

As mentioned before, specimen 5 is held at yield stress for 5 days. After the corrosion, the surface is covered by a shiny black iron oxide layer. A ripple-like texture orthogonal to the direction of the applied stress is visible, as shown in Figure 5.10. Even though the ripple-like texture is still visible after polishing off the iron oxide

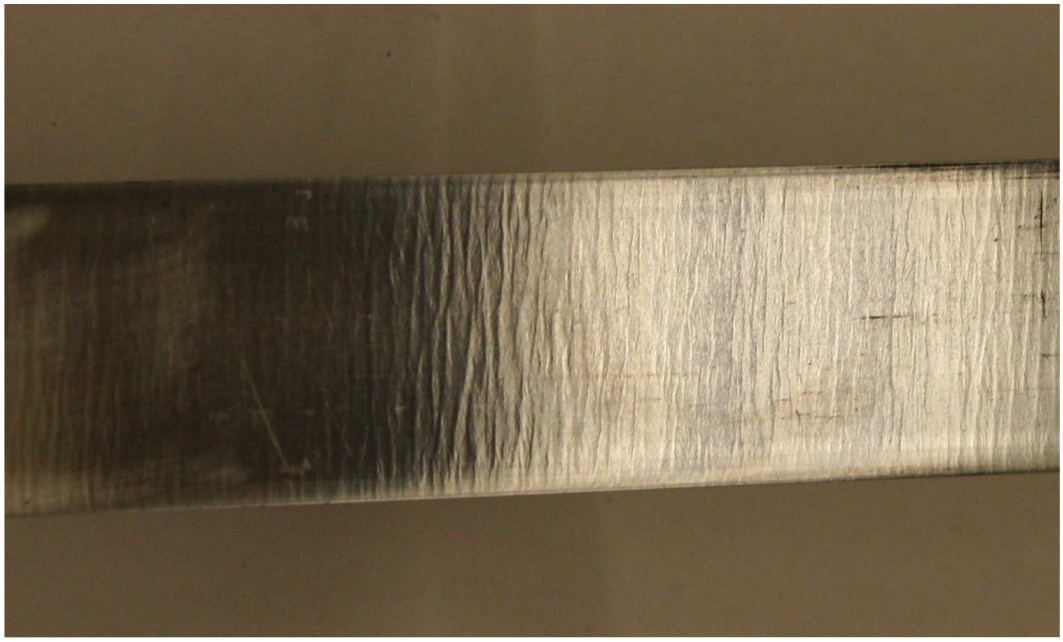

Figure 5.10: Macroscopic surface condition of sample 5

layer, it is not recognizable under the microscope. However, a multitude of cracks are visible under the microscope, even at a smaller magnification, as shown in Figure 5.11. Microscopic examination as described in Section 3.3 reveals an average crack

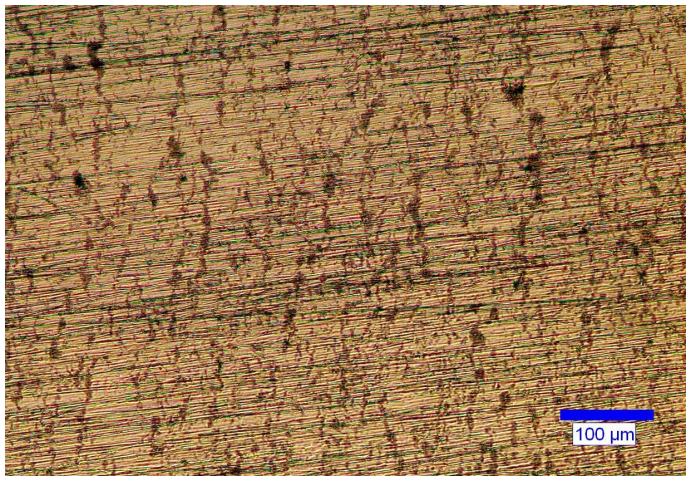

Figure 5.11: Microscopic image of damaged specimen # 5, 100x magnification

density of 37.4 cracks per mm. The length of the cracks obtained using this method ranges from 22 to 86 μm, with an average crack length of 44.9 μm. However, the true length of the cracks cannot be measured, as the width of the images is only 103 μm. In Figure 5.11 it becomes obvious that a lot of these cracks have a length exceeding 300 μm. Figure 5.12 shows a section of the surface at high magnification, revealing many cracks. Note that most of the cracks cross the boundaries of the image, which indicates a longer crack length.

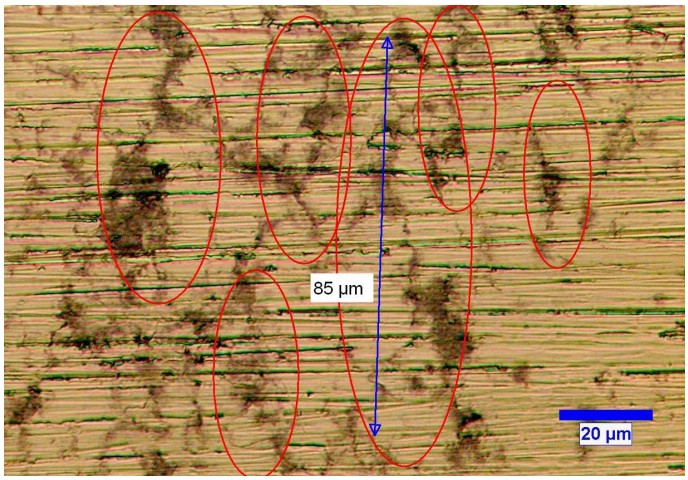

Figure 5.12: Microscopic image of damaged specimen # 5, 500x magnification

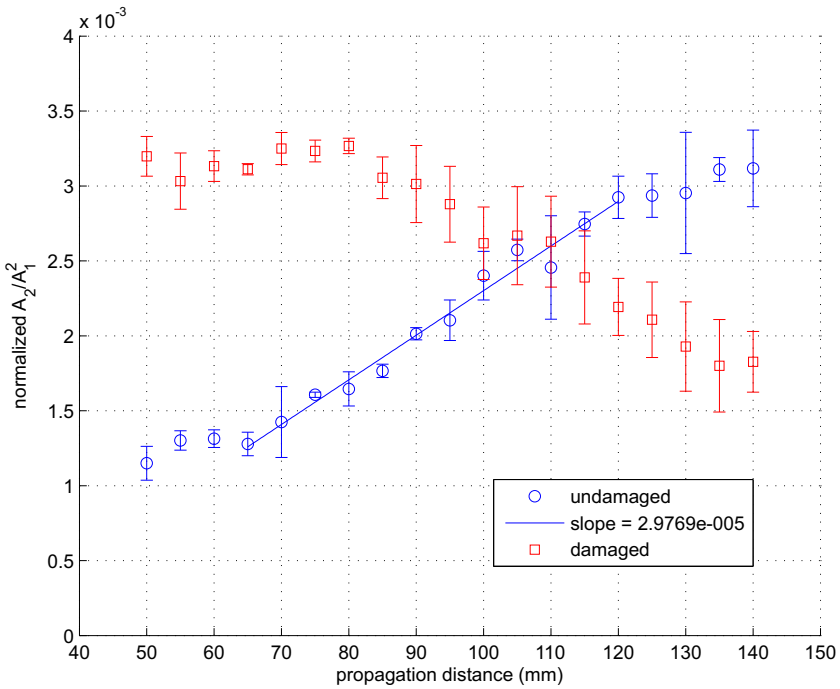

Figure 5.13: Comparison of nonlinearity of undamaged and damaged specimen # 5

5.2.5.2 Ultrasonic Measurement

Figure 5.13 shows the measured nonlinearity of specimen 5 in both the undamaged and damaged conditions. While the specimen in the undamaged condition shows a nonlinear behavior similar to that of the other specimens, in the damaged condition the nonlinearity decreases after a propagation distance of 80 mm. A comparison of the fundamental and second harmonic amplitudes of the specimen in both the undamaged and damaged conditions (Figure 5.14) show a strong decrease of the second harmonic amplitude in damaged condition instead of an increase as in the undamaged condition. A similar effect has been observed by Liu [13]. It seems that the high number of cracks as well as the length and depth of the cracks accounts for the large attenuation and scattering of the second harmonic wave. The ripples on the surface indicate a macroscopic change in the material condition. However, the attenuation behavior of the fundamental wave hardly changes (see Figure 5.14).

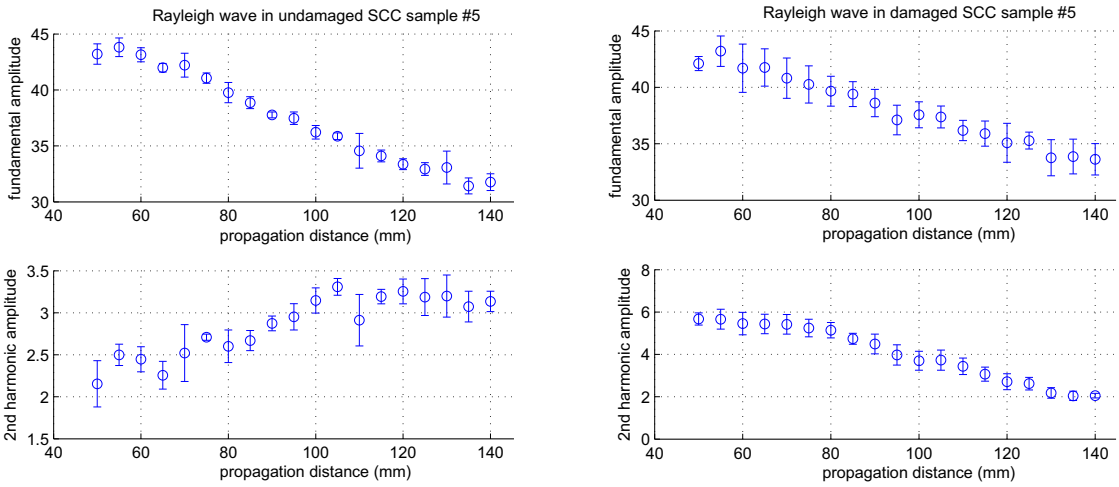

Figure 5.14: Fundamental and second harmonic amplitudes of sample 5 in undamaged condition (left) and damaged condition (right)

5.3 Comparison Between Specimens

Because of the facts mentioned earlier, not all specimens are included in the results. Because of the potentiostat breakdown during the stress corrosion test of specimen 3 and the resulting lack in stress corrosion cracking, this specimen is not included in all of the quantitative comparisons with the other specimens. However, an attempt is made to include the peculiar observations made of this specimen with the other specimens. Due to the obvious differences in material properties between batches 1 and 2 on one hand and batch 3 on the other hand, the results obtained for specimen 5 shall be examined separately.

5.3.1 Change in Nonlinearity with Regard to Applied Stress

For the aforementioned reasons, only the specimens 1, 2, and 4 are considered for this comparison. As there are considerable differences in the absolute value of the nonlinearity parameter even between specimens from the same batch, there is little sense in comparing the absolute values. Instead, the percental change of the nonlinearity parameter of each specimen is used for this comparison. The nominal yield strength, which is 54 ksi, is used as a measure of the amount of accumulated damage. The

nominal yield strength is used instead of the actual yield strength because the latter can not be determined due to the brittle nature of the material (see Section 4.4). The applied stress is a reasonable choice for a measure of damage because it is the only parameter that is changed between individual tests. The results obtained in Section 5.2 are summarized in Table 5.2. This data is visualized in Figure 5.15. Figure 5.15

Table 5.2: Applied stress and results of specimens 1, 2, and 3

Specimen #	tensile stress (in multiples of nominal yield strength)	change in β (in %)
1	1.00	18.9
2	1.078	28.3
4	1.10	31.4

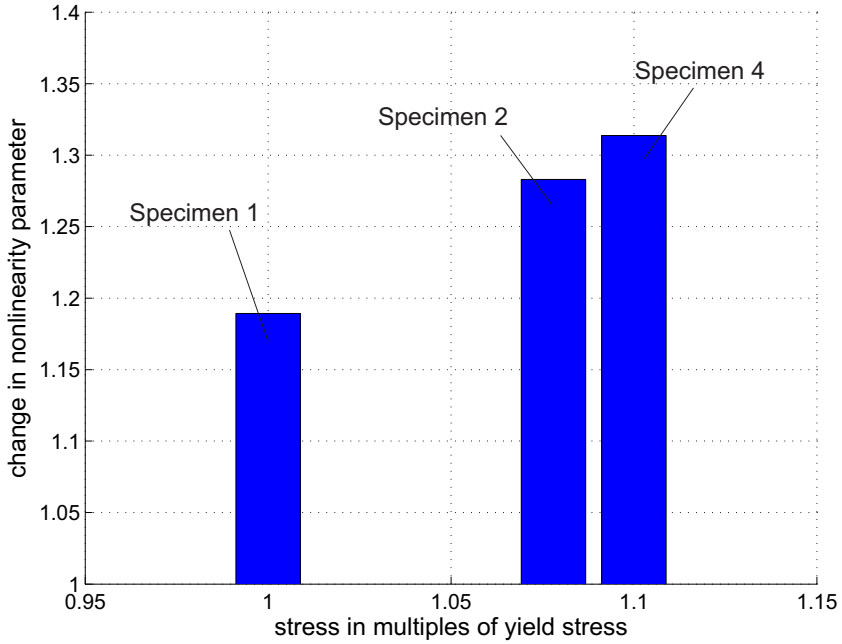

Figure 5.15: Change in β compared to applied stress

shows that there is a clear tendency towards a correlation between the applied tensile stress and the change in the nonlinearity parameter.

5.3.2 Change in Nonlinearity with Respect to Average Crack Density

The applied tensile stress is not necessarily proportional to the actual amount of damage. As mentioned earlier, an attempt was made to quantify the amount of damage on the basis of crack density and crack length. A comparison between the change in the nonlinearity parameter and the crack density, which is experimentally determined by counting the number of cracks visible in 10 adjacent micrographs of the surface and dividing this number by the length of the examined interval, is shown in Figure 5.16. If only specimens 1, 2, and 4 are considered, there seems to be again a corre-

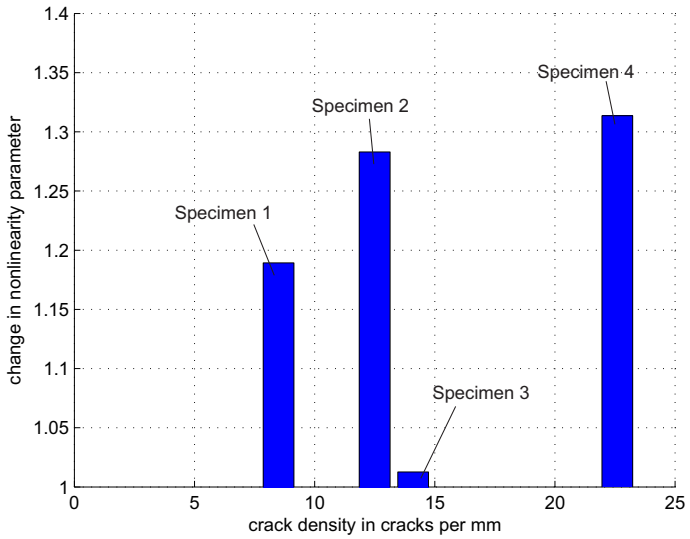

Figure 5.16: Change in β compared to crack density

spondence between the crack density and the change in the nonlinearity parameter. However, this comparison also contains specimen 3, which shows some small cracks. Despite the considerable number of cracks, the change in the nonlinearity parameter of specimen 3 is very small. Therefore, the density of cracks alone seems to be not suitable as a measure of damage. This suggests that the crack size also has an important role in quantifying the damage.

5.3.3 Change in Nonlinearity with Respect to Average Crack Length

It is a plausible assumption that larger cracks indicate more damage. Due to contact or clapping nonlinearity, it can also be assumed that - within a certain range - larger cracks generate a bigger change in the nonlinearity parameter. Figure 5.17 shows a

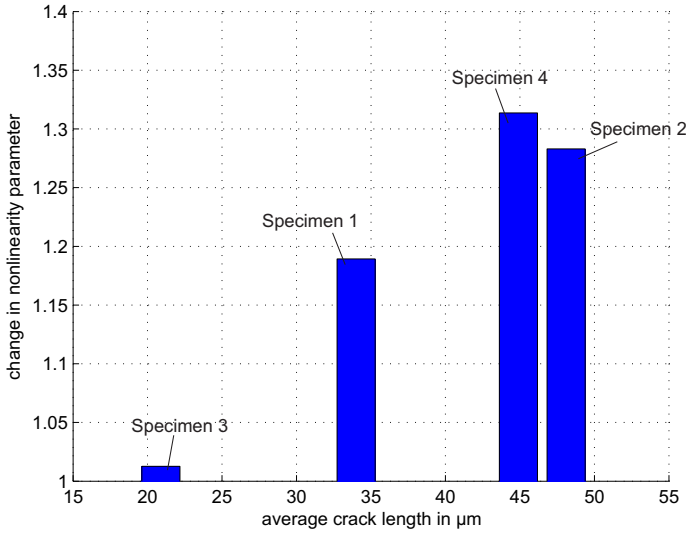

Figure 5.17: Change in β compared to average crack length

comparison between the change in the nonlinearity parameter and the average crack length. Overall, the observed average crack length of less than 50 μm is much smaller than the fundamental and second harmonic wavelengths of 1.32 mm and 0.66 mm, respectively. Therefore, traditional linear ultrasonic techniques based on scattering or attenuation would not work to detect any damage. The average crack length is determined by averaging the length of all cracks visible on the micrographs which are also used for determining the crack density. In this figure, specimen 3 is included to examine the effects of the very small cracks found in this specimen. The figure confirms a general trend that larger crack sizes lead to higher nonlinearity. However, there are some flaws in this reasoning:

The increase in nonlinearity in specimen 3 is very small compared to that of the other specimens, even when the smaller crack size is considered. The reason for this could be that the nonlinearity factor is influenced not only by the cracks, but also by other

microstructural changes like dislocations which are formed in the volume near the crack tips, as described in Section 3.1. Another, more hypothetical, reason could be that only cracks with a length greater than a threshold value contribute significantly to the nonlinearity.

Furthermore, it is noticeable that specimen 4 has a greater change in nonlinearity than specimen 2, even though the average crack size is a bit lower. A reason for this could either be statistical deviations, i.e. the cracks in the examined area are not representative for the whole specimen. Another reason could be that, while the cracks of specimen 4 are indeed slightly smaller than those of specimen 2, this difference is balanced by the greater number of cracks in specimen 4. This possibility raises the need of a parameter that includes both the crack size and the crack density.

5.3.4 Damage Parameter

In this section, a damage parameter as mentioned in the previous section is proposed. As mentioned before, this parameter should include both the crack size and the crack density. It is assumed that both the length and the depth of the crack, or the crack area [16], have an influence on the nonlinear character of the material. As there is an approximately linear relationship between the crack length and the crack depth (see Section 3.3), the length shall be a quadratic factor in the new parameter. Therefore, the damage parameter is defined as

$$p_{dmg} \equiv l^2 \rho, \tag{5.1}$$

where l is the average crack length in μm, and ρ is the (longitudinal) crack density in cracks per mm, measured as described in Section 3.3. The obtained values for the damage parameter of the specimens 1 through 4 can be found in Table 5.3. These results are visualized in Figure 5.18. One can see that for all examined specimens, a higher damage parameter results in a higher change in the nonlinearity parameter. However, specimen 3 still does not perfectly fit in due to the very low change in

Table 5.3: Damage parameter of specimens 1 through 4

Specimen #	avg. crack length l (in μm)	avg. crack density ρ (in 1/mm)	damage parameter p_{dmg} (in m^{-9})
1	34	8.5	9826
2	48.1	12.5	28920
3	20.9	14.1	6159
4	44.9	22.6	45562

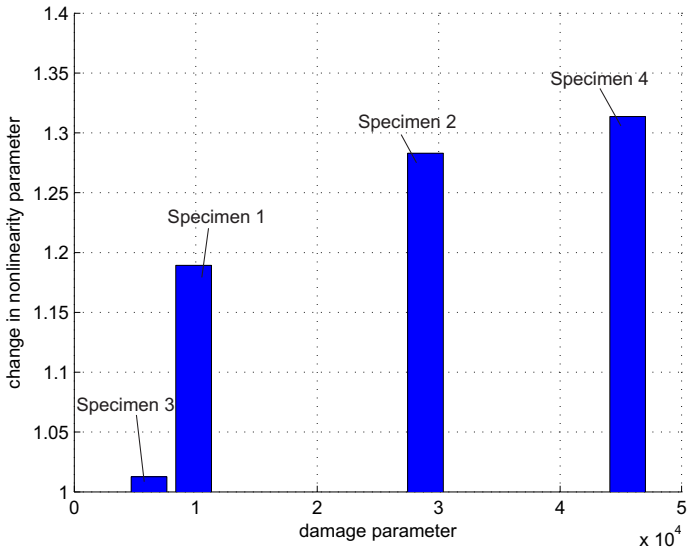

Figure 5.18: Change in β compared to the damage parameter p_{dmg}

nonlinearity. This could mean that judging the amount of damage purely on the basis of the observed microcracks is not sufficient, as there can be cases with recognizable microcracks, but no perceptible change in the nonlinearity parameter. Obviously, the increase in the nonlinearity parameter is caused not only by cracks, but also by microstructural changes like dislocations, which are hardly observable with the microscope.

5.3.5 Examination of specimen 5

Section 5.2.5 shows the unusual nonlinear behavior of specimen 5 and gives possible explanations for this behavior. Now, the significance of the obtained results is discussed briefly. As mentioned earlier, the strength of the material used for specimen 5

is much lower than that of the other specimens, which results in a much higher degree of damage. The ultrasonic measurements show a strong increase in attenuation of the second harmonic, which results in an apparent decrease in nonlinearity - or even a negative nonlinearity parameter - for propagation distances of over 80 mm, which is not consistent with the theory of Chapter 2. Therefore, the evaluation methods used for the other specimens cannot be used for specimen 5. While this makes it impossible to quantitatively compare the results of specimen 5 to those of the other specimens, the peculiar characteristics of the result can nevertheless be used as an indicator for damage. Assuming these results were obtained in a real-life application, the unusual characteristics would be sure to attract the examiner's attention and lead to the detection of the damage.

Therefore, it can be said that an increase in the nonlinearity factor indicates a certain amount of microstructural damage, while nonlinear characteristics like those obtained for specimen 5 indicate a larger amount of micro- and macrostructural damage.

CHAPTER VI

CONCLUSIONS AND OUTLOOK

In this research, damage due to stress corrosion cracking in carbon steel is detected using nonlinear Rayleigh surface waves. Rayleigh waves are successfully generated and detected with the wedge method. In order to obtain the nonlinearity parameter, the propagation distance is varied by placing the receiving wedge at different positions along the path of the wave propagation. With this procedure, the effect of inherent nonlinearities of the measurement instrumentation can be isolated and the material only nonlinearity identified. However, it is prone to inaccuracies due to inconsistent application of the wedge to the specimens, specifically coupling issues. Therefore, it is necessary to average the results of multiple measurements, which makes the procedure very time-consuming.

The results show an increase in the nonlinearity parameter in the damaged specimens which is dependent on the amount of stress corrosion damage. A specimen which is subjected to stress which is large enough to induce SCC in a comparable specimen, but a modified electrochemical environment, shows no significant change in the nonlinearity parameter, even though small microcracks are visible on the surface. However, the reliable detection of stress corrosion damage is only possible for moderate damage levels. In a severely damaged specimen, the attenuation of the second harmonic wave is so high that the second harmonic amplitude actually decreases over the propagation distance. This specific specimen, however, shows changes of the surface condition that are visible to the naked eye, which indicates an advanced level of damage. While this behavior does not show the expected characteristics similar to the other specimens, it does at least stand out as compared to the other specimens

and therefore catches the attention of the examiner. More important than the behavior of the severely corroded specimen, however, is the fact that comparably small levels of damage generate substantial changes in the nonlinearity factor, which means that this kind of damage can be detected before macroscopic changes of the material become visible, which was the objective of this work. In moderately damaged specimens with a constant corrosive environment, the relationship between the measured change in nonlinearity and the applied stress is almost linear. Furthermore, a correlation between both the average crack density and the average crack length and the measured change in the nonlinearity parameter is observed. Therefore, a damage paramterer is proposed to qualitatively explain the behavior of measured nonlinearity versus different factors that influence the nonlinearity. The parameter is based on the assumption that the observed change in nonlinearity is solely due to the cracks.

There are still some issues that can be addressed in future work. First of all, as described above, the procedure of repositioning the wedge is time-consuming and a potential source of error. A method which simplifies this process and reduces inconsistencies would be very helpful. For possible commercial applications of this method, a high degree of automation seems to be necessary. Another potential source of error is the choice of the interval which is to be evaluated. Manual selection of the boundaries between the region of the near field effect and the area of saturation is always affected by subjective criteria. Algorithms which assist the evaluation process to a greater degree or even perform the evaluation could help to further improve the practicability of this method.

When performing further experimental research, some points should be observed to improve the research process. To improve consistency between the individual specimens, enough material should be acquired, so the specimens have exactly the same material properties. It might also be advantageous if the actual material properties resemble the nominal values more closely. The material properties should be verified

before conducting any tests. Furthermore, great attention should be paid to the manufacturing of the specimens. Some manufacturing methods can result in considerable deviations from the specified geometry. It might also be helpful to get the surface automatically polished in order to achieve a constant surface quality.

REFERENCES

[1] Achenbach, J., *Wave propagation in elastic solids*. North-Holland, 1999.

[2] Cantrell, J. H., "Substructural organization, dislocation plasticity and harmonic generation in cyclically stressed wavy slip metals," *Proceedings of the Royal Society of London, Series A*, vol. 460, pp. 757–780, Mar. 2004.

[3] Cantrell, J. H. and Yost, W. T., "Nonlinear ultrasonic characterization of fatigue microstructures," *International Journal of Fatigue*, vol. 23, no. Supplement 1, pp. 487 – 490, 2001.

[4] Cash, W. D. and Cai, W., "Dislocation contribution to acoustic nonlinearity: The effect of orientation-dependent line energy," *Journal of applied Physics*, vol. 109, Jan. 2011.

[5] Chen, Z., Janousek, L., Yusa, N., and Miya, K., "A nondestructive strategy for the distinction of natural fatigue and stress corrosion cracks based on signals from eddy current testing," *Journal of Pressure Vessel Technology*, vol. 129, pp. 719 – 728, 2007.

[6] Graff, K. F., *Wave Motion in Elastic Solids*. New York: Dover Publications, 1991.

[7] Hamilton, M. F. and Blackstock, D. T., *Nonlinear Acoustics*. Academic Press, 1998.

[8] Herrmann, J., Kim, J.-Y., Jacobs, L. J., Qu, J., Littles, J. W., and Savage, M. F., "Assessment of material damage in a nickel-base superalloy using nonlinear Rayleigh surface waves," *Journal of Applied Physics*, vol. 99, no. 12, 2006.

[9] Jones, R. H., *Stress-Corrosion Cracking*. Materials Park, Ohio: ASM International, 1992.

[10] Kim, J.-Y., Jacobs, L. J., Qu, J., and Littles, J. W., "Experimental characterization of fatigue damage in a nickel-base superalloy using nonlinear ultrasonic waves," *Journal of the Acoustical Society of America*, vol. 120, pp. 1266–1273, Sept. 2006.

[11] Kinsler, L. E., Frey, A. R., Coppens, A. B., and Sanders, J. V., *Fundamentals of Acoustics*. New York: John Wiley & Sons, 1999.

[12] Larson, G. D., Martin, J. S., and Scott Jr., W. R., "Seismic landmine detection using microphones as near-ground sensors," *Journal of the Acoustical Society of America*, vol. 117, pp. 2385–2385, Apr. 2005.

[13] Liu, M., Kim, J.-Y., Jacobs, L. J., and Qu, J., "Experimental study of nonlinear Rayleigh wave propagation in shot-peened aluminum plates - Feasibility of measuring residual stress," *NDT&E International*, vol. 44, pp. 67–74, Jan. 2011.

[14] Matlack, K. H., Kim, J.-Y., Jacobs, L. J., Qu, J., and Singh, P. M., "Nonlinear Rayleigh waves to detect initial damage leading to stress corrosion cracking in carbon steel," *Quantitative Nondestructive Evaluation*, 2011.

[15] Nagy, P. B., "Fatigue damage assessment by nonlinear ultrasonic materials characterization," *Ultrasonics*, vol. 36, pp. 375 – 381, 1998.

[16] Nazarov, V. E. and Sutin, A. M., "Nonlinear elastic constants of solids with cracks," *Journal of the Acoustical Society of America*, vol. 102, no. 6, pp. 3349 – 3354, 1997.

[17] Oppenheim, A. V., Schafer, R. W., and Buck, J. R., *Discrete-Time Signal Processing*. Upper Saddle River, New Jersey: Prentice Hall, 1998.

[18] Parkins, R. N., "Stress Corrosion Spectrum," *British Corrosion Journal*, vol. 7, pp. 15–28, Jan. 1972.

[19] Pruell, C., Kim, J.-Y., Qu, J., and Jacobs, L. J., "Evaluation of fatigue damage using nonlinear guided waves," *Smart Materials and Structures*, vol. 18, p. 035003, 2009.

[20] Roos, E. and Maile, K., *Werkstoffkunde für Ingenieure*. Heidelberg: Springer, 2011.

[21] Rose, J. L., *Ultrasonic waves in solid media*. Cambridge, UK: Cambridge University Press, 1999.

[22] Singh, P. M., *Stress Corrosion Cracking of Carbon Steel and Inconel 600*. PhD thesis, University of Newcastle upon Tyne, 1989.

[23] Staehle, R. W., "Comments on the history, engineering and science of stress corrosion cracking," in *Proceedings of Conference Fundamental Aspects of Stress Corrosion Cracking* (Staehle, R. W., Forty, A. J., and van Rooyen, D., eds.), (Houston, Texas), pp. 3 – 14, National Association of Corrosion Engineers, 1967.

[24] Valluri, J. S., Balasubramaniam, K., and Prakash, R. V., "Creep damage characterization using non-linear ultrasonic techniques," *Acta Materialia*, vol. 58, no. 6, pp. 2079 – 2090, 2010.

[25] Viktorov, I. A., *Rayleigh and Lamb waves: physical theory and applications.* New York: Plenum Press, 1967.

[26] Walker, S. V., "Characterization of fatigue damage in A36 steel specimens using nonlinear Rayleigh surface waves," Master's thesis, Georgia Institute of Technology, 2011.

[27] Walker, S. V., Kim, J.-Y., Qu, J., and Jacobs, L. J., "Fatigue damage evaluation in A36 steel using nonlinear Rayleigh surface waves," *NDT&E International*, vol. 48, pp. 10 – 15, 2012.

[28] Zin, F., Wang, Z., and Kishimoto, K., "Basic properties of Rayleigh surface wave propagation along curved surfaces," *International Journal of Engineering Science*, vol. 43, pp. 250–261, Feb. 2005.